Sensorless Control of Induction Machines
– with or without Signal Injection?

Overview Paper

Joachim Holtz, *Fellow, IEEE*
Electrical Machines and Drives Group, University of Wuppertal
42097 Wuppertal – Germany

Abstract — **Controlled induction motor drives without mechanical speed sensors at the motor shaft have the attractions of low cost and high reliability. To replace the sensor, the information on the rotor speed is extracted from measured stator currents and from the voltages at the motor terminals. Vector controlled drives require estimating the magnitude and spatial orientation of the fundamental magnetic flux waves in the stator or in the rotor. Open loop estimators or closed loop observers are used for this purpose. They differ with respect to accuracy, robustness, and sensitivity against model parameter variations. Dynamic performance and steady-state speed accuracy around zero speed range is achieved by signal injection, exploiting the anisotropic properties of the machine. The overview in this paper uses signal flow graphs of complex space vector quantities to provide an insightful description of the systems used in sensorless control of induction motors.**

Keywords: Induction motor, sensorless speed control, sensorless position control, vector control, observers, modelling, identification, adaptive tuning, signal injection

	fundamental model		exploited anisotropies			
additional signal injection	no	no	no	yes	yes	yes/no
principle	open loop models	observers	rotor slot harmonics	main inductance saturation	artificial saliency	rotor slot leakage
minimum frequency	close to, or temporarily zero	close to, or temporarily zero	below 1 Hz	theoret. zero	theoret. zero	zero
max. speed error	half rated slip	half rated slip	theoret. zero	half rated slip	small	theoret. zero
position error	–	–	–	–	–	theoret. zero

Fig. 1. Methods of sensorless speed control

1. INTRODUCTION

Controlled induction motor drives without speed sensor have emerged as a mature technology in the past decade [1, 2]. The advantages of sensorless control are reduced hardware complexity and lower cost, reduced size of the drive machine, elimination of the sensor cable, better noise immunity, increased reliability and less maintenance requirements. A motor without speed sensor is indicated for operation in hostile environments. Notwithstanding the rapid progress at which the new technologies have emerged, the requirement of operating a sensorless drive at very low speed constitutes a persisting challenge.

Fig. 1 gives a schematic overview of the methodologies applied to sensorless speed control. A first category comprises the methods that model the induction motor by its state equations. A sinusoidal flux density distribution in the airgap is then assumed, neglecting space harmonics and other secondary effects. The approach defines the class of fundamental models. They are either implemented as open loop structures, like the stator model, or as closed loop observers. The latter make use of error signals between measured and estimated quantities that are fed back to the observers in order to increase their robustness and improve their dynamics. Fundamental models have their limits at zero stator frequency. The rotor induced voltage is then zero, which renders the induction motor an unobservable system.

It is particularly the low speed range where anisotropic properties of the machine can provide additional information on the field angle or the position of the rotor. Voltages induced in the stator windings by spatial rotor slot harmonics can be utilized to determine accurate speed signals. Transient excitation by injected signals having other frequencies than the fundamental, or the transients caused by inverter switching, serve to detect the spatial orientations of existing anisotropies. The response of the motor is used either to identify the field angle, or the rotor position angle.

Both the fundamental model methods and the signal injection techniques are competing to improve the low speed performance of sensorless drives. This overview paper characterizes the major representatives of either class. It visualizes their functionalities by complex signal flow graphs and discusses their merits and shortcomings.

2. OPEN LOOP MODELS

2.1 The stator model

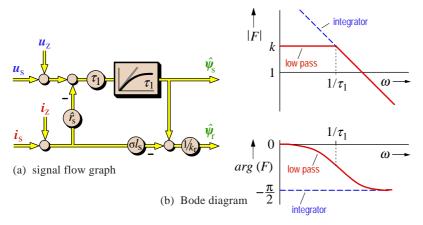The stator model is derived by integrating the stator induced voltage $u_i = u_s - r_s i_s$, which yields

(a) signal flow graph

(b) Bode diagram

Fig. 2. Stator model; the ideal integrator is approximated by a low pass filter

$$\hat{\boldsymbol{\psi}}_s = \int (\hat{\boldsymbol{u}}_s - \hat{r}_s \boldsymbol{i}_s)\,d\tau, \qquad \hat{\boldsymbol{\psi}}_r = \frac{1}{k_r}\left(\hat{\boldsymbol{\psi}}_s - \sigma \hat{l}_s \boldsymbol{i}_s\right) \tag{1}$$

where σl_s is the total leakage inductance, $\sigma = 1 - l_m^2/l_s l_r$ is the total leakage factor, and $k_r = l_m/l_r$ is the coupling factor of the rotor. The resulting stator flux linkage vector $\hat{\boldsymbol{\psi}}_s$ is then used to determine the stator field angle $\hat{\delta}^S = \arg(\hat{\boldsymbol{\psi}}_s)$, or, considering the leakage flux vector $\sigma \hat{l}_s \boldsymbol{i}_s$, the rotor field angle $\hat{\delta}^R = \arg(\hat{\boldsymbol{\psi}}_r)$. Equation (1) is visualized by the signal flow diagram Fig. 2(a), [3]. Note that time is normalized as $\tau = \omega_{sR} t$, where ω_{sR} is the rated stator frequency.

The stator model as defined by (1) is difficult to apply in practice since unavoidable disturbances $\boldsymbol{u}_z$ and $\boldsymbol{i}_z$, invariably superimposed to the acquired signals $\boldsymbol{u}_s$ and $\boldsymbol{i}_s$ in Fig. 2(a), impede achieving the required accuracy. It is particularly the offset and drift effects that arise from analogue signal measurement. They accumulate at the integrator output in Fig. 2(a). The resulting runaway of the output signal is a fundamental problem of an open integration. A negative, low-gain feedback is therefore added which stabilizes the integrator and prevents its output from increasing without bounds. The feedback signal converts the integrator to a first-order delay, designed to have a low corner frequency $1/\tau_1$. The stator model (1) thus becomes

$$\tau_1 \frac{d\hat{\boldsymbol{\psi}}_s}{d\tau} + \hat{\boldsymbol{\psi}}_s = \tau_1(\hat{\boldsymbol{u}}_s - \hat{r}_s \boldsymbol{i}_s) \tag{2}$$

The Bode diagram Fig. 2(b) shows that the first order delay, or low-pass filter, behaves as an integrator for frequencies much higher than the corner frequency. It is obvious that the model becomes inaccurate when the frequency reduces to values around the corner frequency. The gain then reduces and, more importantly, the –90° phase shift of the integrator is lost. This causes an increasing error of the estimated field angle as the stator frequency reduces, which finally makes the system unstable.

The decisive parameter of the stator model is the stator resistance r_s. The resistance of the winding material increases with temperature and can vary in a 1:2 range. A parameter

error in $\hat{r}_s$ affects the signal $\hat{r}_s \boldsymbol{i}_s$ in Fig. 2(a). This signal dominates the integrator input when the magnitude of $\boldsymbol{u}_s$ reduces at low speed. Conversely, it has little effect on the integrator input at higher speed as the nominal value of $r_s i_s$ is then low. Its value ranges between 0.02 - 0.05 p.u., where the lower values apply to high power machines.

To summarize, the stator model is sufficiently robust and accurate at higher stator frequency. Two basic deficiencies let this model degrade as the speed reduces: The integration problem, and the sensitivity of the model to stator resistance mismatch. Depending on the accuracy that can be achieved in a practical implementation, the lower limit of stable operation is reached when the stator frequency is around 1 - 3 Hz.

2.2 Model reference adaptive system

The model reference approach (MRAS) makes use of the redundancy of two machine models of different structures that estimate the same state variable on the basis of different sets of input variables [4]. Both models are referred to in the stationary reference frame. The stator model (2) in the upper portion of Fig. 3 serves as a reference model. Its output is the estimated rotor flux vector $\hat{\boldsymbol{\psi}}_r^S$. The superscript ^{S} indicates that $\hat{\boldsymbol{\psi}}_r$ originates from the stator model.

The rotor model is defined by the differential equation of the rotor winding system [2]

$$\tau_r \frac{d\hat{\boldsymbol{\psi}}_r}{d\tau} + \hat{\boldsymbol{\psi}}_r = j\hat{\omega}_m \hat{\tau}_r \hat{\boldsymbol{\psi}}_r + l_m \boldsymbol{i}_s. \tag{3}$$

This model estimates the rotor flux based on the measured stator current and on a tuning signal, $\hat{\omega}_m$ in Fig. 3. The tuning signal is obtained through a proportional-integral (PI) controller from a scalar error signal $e = \hat{\boldsymbol{\psi}}_r^S \times \hat{\boldsymbol{\psi}}_r^R |_z = \hat{\psi}_r^S \hat{\psi}_r^R \sin \alpha$. This notation denotes the z-component of the vector product. The error signal e is proportional to the angu-
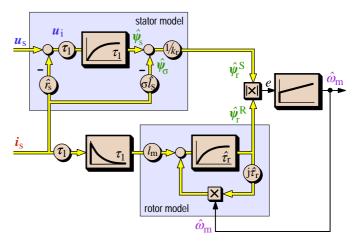

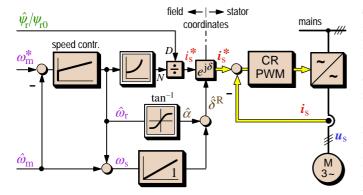Fig. 3. Model reference adaptive system for speed estimation

Fig. 4. Speed and current control systen for MRAS estimators; CR PWM: current regulated pulsewidth modulator; *N*: Numerator, *D*: Denominator

lar displacement α between the two estimated flux vectors. As the error signal gets minimized by the PI controller, the tuning signal $\hat{\omega}_\mathrm{m}$ approaches the actual speed ω_m of the motor. The rotor model as the adjustable model then aligns its output vector $\hat{\boldsymbol{\psi}}_\mathrm{r}^\mathrm{R}$ with the output vector $\hat{\boldsymbol{\psi}}_\mathrm{r}^\mathrm{S}$ of the reference model.

The low-pass approximation (2) of the ideal stator model (1) makes the integration ineffective in the frequency range around and below $1/\tau_1$. It necessitates the addition of an equivalent bandwidth limiter in the input of the adjustable rotor model. Below the cutoff frequency $\omega_\mathrm{sR}/\tau_1 \approx 1\text{ - }3$ Hz, speed estimation becomes therefore inaccurate. A reversal of speed through zero in the course of a transient process is nevertheless possible, if such process is fast enough not to permit the output of the τ_1-delay element (2) to assume erroneous values. However, if the drive is operated at close to zero stator frequency for a longer period of time, the estimated flux goes astray and speed estimation is lost.

According to [4], a speed control system can be superimposed to the speed estimator as shown in Fig. 4. The estimated speed signal $\hat{\omega}_\mathrm{m}$ is supplied by the model reference adaptive system Fig. 3. The speed controller in Fig. 4 generates a rotor frequency signal $\hat{\omega}_\mathrm{r}$, which controls the stator current magnitude

$$i_\mathrm{s} = \frac{\hat{\psi}_\mathrm{r0}}{l_\mathrm{s}}\sqrt{1 + \hat{\omega}_\mathrm{r}^{\,2}\hat{\tau}_\mathrm{r}^{\,2}}\ , \qquad (4)$$

in the base speed range and the current phase angle

$$\delta^\mathrm{R} = \int \hat{\omega}_\mathrm{s}d\tau + tan^{-1}\big(\hat{\omega}_\mathrm{r}\hat{\tau}_\mathrm{r}\big), \qquad (5)$$

both at rotor field orientation. Equations (4) and (5) are derived from the condition for rotor field orientation [2]

$$l_\mathrm{m}i_\mathrm{q} = \omega_\mathrm{r}\tau_\mathrm{r}\psi_\mathrm{rd} \qquad (6)$$

and from the steady-state solution $i_\mathrm{d} = \psi_\mathrm{r}/l_\mathrm{m}$ of (3) in field coordinates, where $\psi_\mathrm{rq} \approx 0$, and hence $\psi_\mathrm{rd} = \psi_\mathrm{r}$ is assumed for existing field orientation. The signal $\psi_\mathrm{r}/\psi_\mathrm{r0}$ in Fig. 4 increas-

es the stator current reference at field weakening. This linearizes the speed control loop; ψ_r0 is the normalized rotor flux linkage in the base speed range.

It is a particular asset of the approach [4] that an accurate orientation of the injected current vector is maintained even if the model value of $\hat{\tau}_\mathrm{r}$ differs from the actual rotor time constant of the machine. The reason is that the same, even erroneous value of $\hat{\tau}_\mathrm{r}$ is used both in the rotor model (3) and in the algorithm (4) and (5) of the speed control scheme Fig. 4. If the tuning controller in Fig. 3 maintains zero error, the control scheme exactly replicates the same dynamic relationship between the stator current vector and the rotor flux vector that exists in the actual motor, even in the presence of a rotor time constant error [4]. However, the accuracy of speed estimation, reflected in the feedback signal $\hat{\omega}_\mathrm{m}$ to the speed controller, is degraded by an error in $\hat{\tau}_\mathrm{r}$.

A more severe source of inaccuracy is a possible mismatch of the reference model parameters, particularly of the stator resistance r_s. Good dynamic performance of the system is reported by *Schauder* above 2 Hz stator frequency [4].

2.3 Rotor field orientation with improved stator model

A sensorless rotor field orientation scheme based on the stator model is described by *Ohtani* [5]. The upper portion of Fig. 5 shows the classical structure in which the controllers for speed and rotor flux generate the current reference vector $\boldsymbol{i}_\mathrm{s}^*$ in field coordinates. This signal is transformed to stator coordinates and processed by a current regulated pulsewidth controller (CR PWM). A possible misalignment of the reference frame is detected as the difference of the measured q-axis current from its reference value i_q^*. This error signal feeds a PI controller, the output of which is the estimated mechanical speed. It is added to an estimated value $\hat{\omega}_\mathrm{r}$ of the rotor
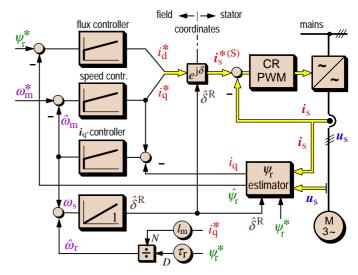

Fig. 5. Sensorless speed control based on direct i_q estimation and rotor field orientation. CR PWM: Current regulated pulsewidth modulator; *N*: Numerator, *D*: Denominator
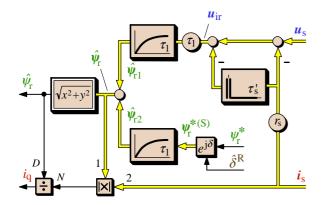
Fig. 6. Rotor flux estimator for the structure in Fig. 5; N: Numerator, D: Denumerator

frequency, obtained with reference to the condition for rotor field orientation (6), but computed from the reference values i_q^* and ψ_r^*. The reason is that the measured value i_q is usually contaminated by inverter harmonics, while the estimated rotor flux linkage vector $\hat{\boldsymbol{\psi}}_r$ is erroneous at low speed. The integration of ω_s provides the rotor field angle $\hat{\delta}^R$.

The stator model is used to estimate the rotor flux vector $\boldsymbol{\psi}_r$. The drift problems of an open integration at low frequency are avoided in Fig. 6 by band-limited integration by means of a first-order delay. This entails a severe loss of gain in $\boldsymbol{\psi}_r$ at low stator frequency, while the estimated field angle deviates considerably form the actual position of the rotor field. The Bode plot in Fig. 2(b) demonstrates these effects.

An improvement is brought about by the following considerations. The transfer function of an integrator is

$$\tilde{\boldsymbol{\psi}}_r = \frac{1}{s}\tilde{\boldsymbol{u}}_{ir} = \frac{1}{s}\tilde{\boldsymbol{u}}_{ir}\frac{\tau_1 s+1}{\tau_1 s+1} \qquad (7)$$

where $\tilde{\boldsymbol{\psi}}_r$ and $\tilde{\boldsymbol{u}}_{ir}$ are the Laplace transforms of the respective space vectors, and $\boldsymbol{u}_{ir}$ is the rotor induced voltage in the stator windings. The term in the right is expanded by a fraction of unity value. The expression is then decomposed

$$\tilde{\boldsymbol{\psi}}_r = \frac{\tau_1}{\tau_1 s+1}\tilde{\boldsymbol{u}}_{ir} + \frac{1}{\tau_1 s+1}\cdot\tilde{\boldsymbol{\psi}}_r^* = \tilde{\boldsymbol{\psi}}_{r1}+\tilde{\boldsymbol{\psi}}_{r2} \qquad (8)$$

while substituting $\tilde{\boldsymbol{u}}_{ir}/s = \tilde{\boldsymbol{\psi}}_r$ which follows from (7). The result is the equivalent of the pure integral of $\hat{\boldsymbol{u}}_{ir}$, on condition that $\tilde{\boldsymbol{\psi}}_r = \tilde{\boldsymbol{\psi}}_r^*$. A transformation to the time domain yields two differential equations

$$\tau_1\frac{d\boldsymbol{\psi}_{r1}}{d\tau}+\boldsymbol{\psi}_{r1} = \tau_1\left(\boldsymbol{u}_s - r_s\boldsymbol{i}_s - r_s\tau'_s\frac{d\boldsymbol{i}_s}{d\tau}\right), \qquad (9)$$

where $\boldsymbol{u}_{ir}$ is expressed by the measured values of the terminal voltages and currents, written in brackets, and

$$\tau_1\frac{d\boldsymbol{\psi}_{r2}}{d\tau}+\boldsymbol{\psi}_{r2} = \boldsymbol{\psi}_r^{*(S)}. \qquad (10)$$

It is specifically marked here by a superscript that $\boldsymbol{\psi}_r^{*(S)}$ is

referred to in stator coordinates and hence is an ac variable, the same as the other variables.

The signal flow graph Fig. 6 shows that the rotor flux vector is synthesized by the two components $\hat{\boldsymbol{\psi}}_{r1}$ and $\hat{\boldsymbol{\psi}}_{r2}$, according to (9) and (10). The high amplitude of $\boldsymbol{u}_s$ lets $\hat{\boldsymbol{\psi}}_{r1}$ dominate the estimated rotor flux vector $\hat{\boldsymbol{\psi}}_r$ at higher frequencies. As the stator frequency reduces, the amplitude of $\boldsymbol{u}_s$ reduces and $\hat{\boldsymbol{\psi}}_r$ gets increasingly determined by the signal $\hat{\boldsymbol{\psi}}_{r2}$ that is contributed by the lower channel. Since $\boldsymbol{\psi}_r^*$ is the input variable of this channel, the estimated value of $\hat{\boldsymbol{\psi}}_r$ gets replaced by its reference value $\boldsymbol{\psi}_r^*$ in a smooth transition. Finally, we have $\hat{\boldsymbol{\psi}}_r \approx \boldsymbol{\psi}_r^*$ at low frequencies which, in effect, deactivates the rotor flux controller. Still, the field angle $\hat{\delta}^R$ as the argument of the rotor flux vector is under control through the speed controller and the i_q-controller in Fig. 5, although the accuracy of $\hat{\delta}^R$ reduces. Field orientation is finally lost at very low stator frequency, because only the frequency of the stator currents remains controlled. The currents are forced into the machine without reference to the rotor field, $\hat{\delta}^R$ being ill defined. This provides robustness and stability, although not dynamic performance. In fact, the q-axis current i_q is directly derived in Fig. 6 as the current component in quadrature with what is considered the estimated rotor flux vector

$$i_q = \frac{1}{\hat{\psi}_r}\hat{\boldsymbol{\psi}}_r\times\boldsymbol{i}_s\Big|_z, \qquad (11)$$

independently of whether the argument of this vector is correctly estimated. Equation (11) is visualized in the lower left portion of the signal flow diagram Fig. 6.

As the speed increases again, rotor flux estimation becomes more accurate and closed loop rotor flux control is resumed. The correct value of the field angle is readjusted as the q-axis current, through (11), now relates to the correct rotor flux vector. The i_q-controller then adjusts the estimated speed, and in consequence also the field angle for a realignment of the reference frame with the rotor field.

At 18 rpm, speed accuracy is reported to be within ± 3 rpm with a 4-pole machine. Torque accuracy at 18 rpm is about ± 0.03 pu. at 0.1 pu. reference torque, improving significantly as the torque increases. Minimum parameter sensitivity exists at $\tau_1 = \tau_r$ [5].

2.4 Improved stator model for low speed performance

2.4.1 Signal acquisition errors

The basic limitation for very low speed operation is owed to unavoidable dc offset components in the stator current and voltage acquisition channels. These accumulate when being integrated in a flux estimator, producing a drift of the output signal. Some improvement may be obtained by limiting the flux signal to its nominal magnitude. The field angle $\hat{\delta}^S$ as the argument of the stator flux vector $\hat{\boldsymbol{\psi}}_s$ then gets distorted twice per fundamental frequency, which introduces a ripple component in the torque producing current i_q. The resulting
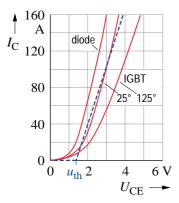
Fig. 7. Forward characteristics of the power devices; dotted line: modelled approximation

At lower speed, also the voltage distortions introduced by the nonlinear behavior of the PWM inverter become significant. These are caused by the forward voltage of the power devices. The respective characteristics are shown in Fig. 7. They can be modelled by an average threshold voltage u_{th}, and an average differential resistance r_d as marked by the dotted line in Fig. 7. A more accurate model is used in [7].

The differential resistance r_d appears in series with the machine winding; its value therefore adds to the stator resistance of the machine model, which is just a change of the model parameter. Other than this, the influence of the threshold voltage is a nonlinear function of the device currents. This calls for defining a nonlinear model of the inverter.

As seen from the inverter, each of the three phase currents i_a, i_b and i_c, flow either through an active device, or through a recovery diode, depending on the inverter switching state. Invariably do the signs of the threshold voltages, being part of the forward voltage drops, coincide with the signs of the respective device currents. The directions of the phase currents do not change during a time interval of one sixth of a

speed oscillations may eventually render the system unstable since the effect gets more and more pronounced when the stator frequency reduces [2].

2.4.2 PWM inverter model
One of the reasons that render a PWM inverter a nonlinear system is the dead-time effect. Means of compensating this disturbance are well known [6]. Their implementation in a sensorless drive is mandatory.

fundamental cycle. Neither does the effect of the device threshold voltages change, even when the switching states change in the ongoing process of pulsewidth modulation. The inverter therefore introduces voltage components of identical magnitude u_{th} to all three phases, with their signs being determined by the directions of the respective phase currents. Describing the device voltages by a voltage space vector defines the threshold voltage vector

$$\boldsymbol{u}_{th} = \frac{1}{2}\big(u_{th}\text{sign}(i_a) + a\,u_{th}\text{sign}(i_b)+a^2 u_{th}\text{sign}(i_c)\big), \quad (12)$$

where a $= exp(j2\pi/3)$. To separate the influence of the stator currents, (12) is expressed as

$$\boldsymbol{u}_{th} = u_{th}\cdot \boldsymbol{sec}(\boldsymbol{i}_s), \quad (13)$$

where

$$\boldsymbol{sec}(\boldsymbol{i}_s) = \frac{1}{2}\big(\text{sign}(i_a) + a\,\text{sign}(i_b) + a^2\text{sign}(i_c)\big) \quad (14)$$

is the sector indicator [8], a complex nonlinear function of $\boldsymbol{i}_s(t)$ having unity magnitude. The sector indicator marks the respective ±30°-sector in which $\boldsymbol{i}_s$ is located. Fig. 8 shows the six discrete locations that the sector indicator $\boldsymbol{sec}(\boldsymbol{i}_s)$ can assume in the complex plane.

The reference signal $\boldsymbol{u}^*$ of the pulsewidth modulator controls the stator voltages of the machine. It follows a circular trajectory in the steady-state. Owing to the threshold voltages of the power devices, the average value $\boldsymbol{u}_{av}$ of the stator voltage vector $\boldsymbol{u}_s$, taken over a modulation cycle, describes trajectories that result distorted and discontinuous. Fig. 9 shows that the fundamental amplitude of $\boldsymbol{u}_{av}$ is less than its reference value $\boldsymbol{u}^*$ at motoring; it is larger at regeneration. The voltage trajectories exhibit strong sixth harmonic components in addition. Since the threshold voltage does not vary with stator frequency as the stator voltage does, the distortions are more pronounced when the stator frequency, and hence also the stator voltages, are low. The distortions may even exceed the commanded voltage in magnitude, which then makes correct flux estimation and stable operation of the drive impossible.

Using the definitions (13) and (14), an estimated value $\hat{\boldsymbol{u}}_s$ of the stator voltage vector is obtained from the PWM reference voltage vector $\boldsymbol{u}_{pwm}$

$$\hat{\boldsymbol{u}}_s = \boldsymbol{u}_{pwm} - \big(\hat{\boldsymbol{u}}_{th} + \hat{r}_d\boldsymbol{i}_s\big), \quad (15)$$

where the term in brackets represents the inverter voltage vector $\boldsymbol{u}_{inv}$. This vector reflects the respective influence of the threshold volt-

Fig. 8. The six possible locations of the sector indicator $\boldsymbol{sec}(\boldsymbol{i}_s)$; the dotted lines indicate the transitions at which the signs of the respective phase currents change
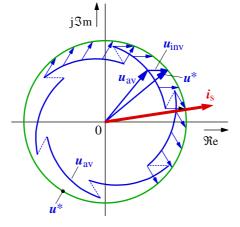

Fig. 9. Trajectories $\boldsymbol{u}_{av}$ of the average stator voltage vector as influenced by the inverter nonlinearity (switching harmonics excluded)

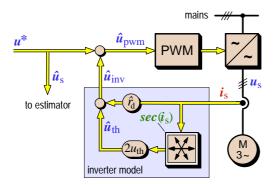Fig. 10. Motor control with linearized PWM inverter

ages through u_{th}, and of the resistive voltage drop $r_d i_s$. A signal flow graph of a motor drive using the linearized inverter model (15) is shown in Fig. 10. Apart from parameter errors, the estimated stator voltage vector $\hat{u}_s$ represents the real voltage quantities at the machine terminals. It is favorable that $\hat{u}_s$ is not contaminated by the switching harmonics that exist in u_s.

2.4.3 Identification of the inverter model parameters

The threshold voltage u_{th} can be identified during self-commissioning from the distortions of the reference voltage vector u^* [7, 8]. In this process, the components u_α^* and u_β^* of the reference voltage vector are acquired with the current controllers injecting sinusoidal currents of very low frequency into the stator windings. In such condition, the machine impedance is dominated by the stator resistance. The stator voltages are then proportional to the stator currents.

Deviations from a sinewave of the reference voltages that control the pulsewidth modulator are therefore caused by the inverter. They are detected by substracting the fundamental components from the reference voltages, which then yields
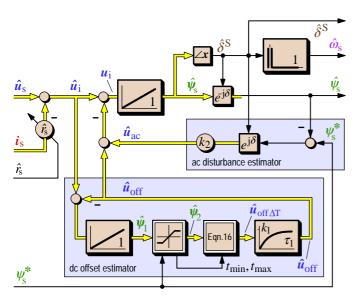
square wave like, stepped waveforms. The voltage steps are proportional to u_{th}. The fundamental components are determined by fast Fourier transform [2].

The differential resistance of the power devices, r_d in (15), establishes a linear relation between the load current and its influence on the inverter voltage. Functionally, it adds to the resistance r_s of the stator windings and hence influences also upon the transient stator time constant of the induction motor, and on the design parameters of the current controllers. The value $(r_s + r_d)$ is estimated by one of the on-line tuning methods described in Section 4.

2.4.4 Stator flux estimation employing a pure integrator

According to (1), the stator flux vector is defined as the integral of the stator induced voltage $\hat{u}_i = \hat{u}_s - \hat{r}_s \hat{i}_s$. As apparent from Fig. 2(a), even minor dc components in the voltage and current signals accumulate in the process of an open integration to form a substantial offset in the estimated stator flux linkage vector. A solution to this problem exploits the fact that the offset vector is unidirectional over a large time interval, while the uncorrupted vector u_i rotates.

The signal flow diagram Fig. 11 shows the elements of a dc offset estimator, highlighted by the lower shaded frame. The estimated stator voltage (15) serves as the input signal $\hat{u}_s$. The vector $\hat{u}_i$ of the induced voltage is integrated to form a signal $\hat{\psi}_1$. The components of this vector are subsequently limited in amplitude to the magnitude value ψ_s^* of the stator flux reference.

The trajectory of the limited vector $\hat{\psi}_2$ is not circular in the presence of dc offset. Since its undisturbed radius equals ψ_s^* through the action of the stator flux controller, the offset components tend to drive the trajectory as a whole towards one of the $\pm\psi_s^*$-boundaries, which makes a clearance appear from the respective boundaries at the opposed sides. Fig. 12 shows an oscillographed example. It is seen that the offset makes the average values of the flux components $\psi_{2\alpha}$ and $\psi_{2\beta}$ nonzero. In particular, we have $(\psi_{2\alpha\,min} + \psi_{2\alpha\,max})/2 < 0$ and $(\psi_{2\beta\,min} + \psi_{2\beta\,max})/2 > 0$ in this example. Hence a contribu-

Fig. 11. Stator flux estimator using a pure integrator; separate estimators are employed for dc offset and ac disturbances
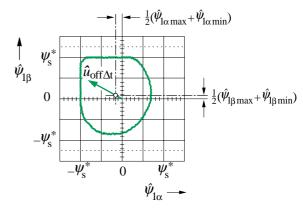

Fig. 12. Recorded trajectory of the vector $\hat{\psi}_1$ showing the effect of uncompensated offset
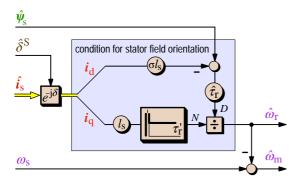
Fig. 13. Speed and rotor frequency estimator

tion $\hat{u}_{off\Delta t}$ to the offset voltage vector can be estimated from the displacement of the flux trajectory $\hat{\psi}_2$ as

$$\hat{u}_{off\,\Delta t} = \frac{1}{\Delta t}\left(\hat{\psi}_{2\,max} + \hat{\psi}_{2\,min}\right) \tag{16}$$

where the maximum and minimum values in (16) are those of the respective components $\psi_{2\alpha}$ and $\psi_{2\beta}$, and Δt is the time difference between two zero crossings of $\hat{\psi}_2$ and thus defines half a fundamental period.

Due to the nonlinear distortion of the trajectory of $\hat{\psi}_2$, the algorithm (16) is only an approximation under the conditions shown in Fig. 12. To improve on this, the signal $\hat{u}_{off\Delta t}$ is low-pass filtered and fed back to the input of the integrator so as to cancel the offset component in $\hat{u}_i$. The input of the integrator then tends towards zero in a quasi steady-state, which makes the estimated offset voltage vector $\hat{u}_{off}$ equal the existing offset in $\hat{u}_i$. The trajectory of $\hat{\psi}_2$ becomes exactly circular in this condition which ensures a precise tracking of the offset voltage vector. The response time of the offset estimator is not at all critical since offset drift is mainly a thermal effect, and hence the dc offset changes very slowly.

With all dc components removed from the estimated induced voltage, the stator flux linkage vector can be obtained by pure integration as per (1). The scheme avoids the low speed estimation error and the bandwidth limitations associated with the low-pass filter approximation (2).
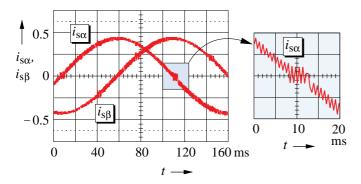

Fig. 14. Measured stator current waveforms to illustrate the zero crossing effect

To complete the stator flux estimator Fig. 11, a rotor frequency signal ω_r is derived from the condition for stator field orientation [2]

$$l_s\left(\tau_r'\frac{di_q}{d\tau} + i_q\right) = \omega_r\tau_r(\psi_s - \sigma l_s i_d) \tag{17}$$

which then permits calculating the mechanical speed as $\omega_m = \omega_s - \omega_r$. In (17), $\tau_r' = \sigma\tau_r$ is the transient rotor time constant and $\sigma = 1 - l_m^2/l_s l_r$ is the total leakage coefficient. A signal flow graph of the speed and rotor frequency estimator is shown in Fig. 13.

2.4.5 Compensation of residual estimation errors

Exact modelling of the PWM inverter is further impaired by a variety of additional effects. One is related to the phenomena that occur when the fundamental components of the phase currents reverse their directions. The exact point of zero crossing is ill defined in the presence of switching harmonics. When a particular phase current reverses, the voltage error caused by the dead-time effect changes its sign and thus counteracts the tendency of this current to flow in the intended direction. The situation is even more complex as the superimposed switching harmonics establish repetitive changes between positive and negative current flow as illustrated in Fig. 14. Dead-time error compensation schemes fail to operate properly.

Another effect superimposes at current zero crossing: The respective bridge arm remains open-circuited once the current has come to zero, and the estimation of the corresponding phase voltage is subsequently lost. It is then the induced voltage of the machine that appears temporarily at this phase terminal. Estimating the exact stator voltage vector from the command value of the pulsewidth modulator then becomes difficult.

The zero crossing effects in total produce distortions of the estimated flux vector signal that are dominated by multiple of six harmonics.

As the signal level of the induced voltage reduces at low speed, also data acquisition errors become significant [8]. The current transducers convert the machine currents to voltage signals that are digitized by analog-to-digital (A/D) converters. Parasitic dc offset components that superimpose to the analog signals appear as ac components of fundamental frequency after their transformation to synchronous coordinates.

Unbalanced gains of the current acquisition channels map a circular current trajectory into an elliptic shape. The magnitude of the current vector then varies at twice the fundamental frequency.

All residual estimation and signal acquisition errors generate ac disturbances of fundamental frequency and higher. An efficient way to minimize their impact on the estimated flux vector is adjusting the radial component of $\hat{\psi}_s$ close to its reference value ψ_s^* by fast proportional closed loop control. This
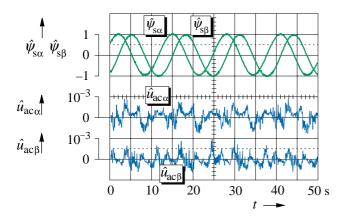
Fig. 15. Measured components of the high-frequency disturbances

leaves the tangential component – the field angle – unaffected and thus does not interfere with the correct operation of the estimator. In a favorable manner, a tangential error converts to a radial error after a quarter revolution of the flux vector and is then eliminated.

The ac disturbance compensator shown in the upper shaded frame in Fig. 11 generates the high-frequency signal $\hat{\boldsymbol{u}}_{ac}$ to serve this purpose. The oscillogram Fig. 15 shows that the components of $\hat{\boldsymbol{u}}_{ac}$, although very small in amplitude, exhibit dominant 6th-order harmonics as predicted, and other high-frequency noise in addition.

Considering all compensation signals, the defining equation of the stator flux estimator in Fig. 11 becomes

$$\hat{\boldsymbol{\psi}}_{s} = \int (\hat{\boldsymbol{u}}_{s} - \hat{r}_{s}\boldsymbol{i}_{s} - \hat{\boldsymbol{u}}_{off} - \hat{\boldsymbol{u}}_{ac})d\tau, \qquad (18)$$

where the dc offset voltage vector is obtained from (16)

$$\hat{\boldsymbol{u}}_{off} = \frac{k_1}{\tau_1}\int (\hat{\boldsymbol{u}}_{off\,\Delta t} - \hat{\boldsymbol{u}}_{off}), \qquad (19)$$

and the estimated ac disturbance vector is

$$\hat{\boldsymbol{u}}_{ac} = k_2 (\boldsymbol{\psi}_{s}^{*} - \hat{\boldsymbol{\psi}}_{s})e^{j\hat{\delta}^{S}} \qquad (20)$$

where $\hat{\delta}^{S}$ is the estimated stator field angle.

3. Closed Loop Observers

The accuracy of the open loop estimation models described in the previous chapters reduces as the mechanical speed reduces. The limit of acceptable performance depends on how precisely the model parameters can be matched to the corresponding parameters of the actual machine. It is particularly at lower speed that parameter errors have significant influence on the steady-state and dynamic performance of the drive system.

The robustness against parameter mismatch and signal noise can be improved by employing closed loop observers to estimate the state variables, and the system parameters.

3.1 Full order nonlinear observer

A full order observer can be constructed from the machine equations in stator coordinates

$$\tau_{\sigma}' \frac{d\boldsymbol{i}_{s}}{d\tau} + \boldsymbol{i}_{s} = \frac{k_{r}}{r_{\sigma}\tau_{r}}(1 - j\omega_{m}\tau_{r})\boldsymbol{\psi}_{r} + \frac{1}{r_{\sigma}}\boldsymbol{u}_{s} \qquad (21a)$$

$$\tau_{r} \frac{d\boldsymbol{\psi}_{r}}{d\tau} + \boldsymbol{\psi}_{r} = j\omega_{m}\tau_{r}\boldsymbol{\psi}_{r} + l_{m}\boldsymbol{i}_{s} \qquad (21b)$$

where $\tau_{\sigma}' = \sigma l_{s}/r_{\sigma}$ is a transient stator time constant, $\tau_{r} = l_{r}/r_{r}$ is the rotor time constant, and $r_{\sigma} = r_{s} + k_{r}^{2}r_{r}$ is an equivalent resistance, and $k_{r} = l_{m}/l_{r}$ is the coupling factor of the rotor. Equations (21) are visualized in the upper portion of Fig. 16. The model outputs are the estimated values $\hat{\boldsymbol{i}}_{s}$ and $\hat{\boldsymbol{\psi}}_{r}$ of the stator current vector and the rotor flux linkage vector, respectively.

Adding an error compensator to the model establishes the observer. An error vector $\Delta\boldsymbol{i}_{s} = \hat{\boldsymbol{i}}_{s} - \boldsymbol{i}_{s}$ is computed from the model current and the measured machine current. It is used to generate correcting inputs to the electromagnetic subsystems that represent the stator and the rotor in the machine model. The equations of the full order observer are then established in accordance with (21). We have

$$\hat{\tau}_{\sigma}' \frac{d\hat{\boldsymbol{i}}_{s}}{d\tau} + \hat{\boldsymbol{i}}_{s} = \frac{k_{r}}{\hat{r}_{\sigma}\hat{\tau}_{r}}(1 - j\hat{\omega}_{m}\hat{\tau}_{r})\hat{\boldsymbol{\psi}}_{r} + \frac{1}{\hat{r}_{\sigma}}\boldsymbol{u}_{s} - \boldsymbol{G}_{s}(\hat{\omega}_{m})\Delta\boldsymbol{i}_{s} \quad (22a)$$

$$\hat{\tau}_{r} \frac{d\hat{\boldsymbol{\psi}}_{r}}{d\tau} + \hat{\boldsymbol{\psi}}_{r} = j\hat{\omega}_{m}\hat{\tau}_{r}\boldsymbol{\psi}_{r} + l_{h}\hat{\boldsymbol{i}}_{s} - \boldsymbol{G}_{r}(\hat{\omega}_{m})\Delta\boldsymbol{i}_{s} \qquad (22b)$$

Kubota et al. [9] select the complex gain factors $\boldsymbol{G}_{s}(\hat{\omega})$ and $\boldsymbol{G}_{r}(\hat{\omega})$ such that the two complex eigenvalues of the observer $\lambda_{1,2\,obs} = k \cdot \lambda_{1,2\,mach}$, where $\lambda_{1,2\,mach}$ are the machine eigenvalues, and k is a real constant. The value of $k > 1$ scales the observer by pole placement to be dynamically faster than the machine. Given the nonlinearity of the system, the resulting
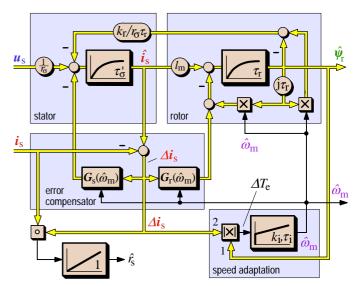

Fig. 16. Full order nonlinear observer; the dynamic model of the electromagnetic subsystem is shown in the upper portion
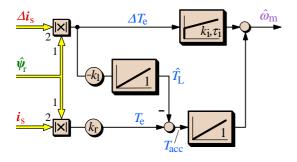
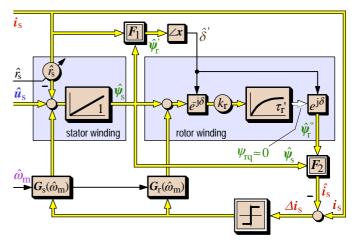Fig. 17. Improved speed adaptation scheme using a load torque estimator

Fig.18. Sliding mode observer;
the functions are $F_1 \equiv \hat{\psi}_r' = (\hat{\psi}_s - \sigma l_s i_s)/k_r$, $F_2 \equiv \hat{i}_s = (\hat{\psi}_s - k_r \hat{\psi}_r'')/\sigma l_s$

complex gains $G_s(\hat{\omega}_m)$ and $G_r(\hat{\omega}_m)$ in Fig. 16 depend on the estimated angular mechanical speed $\hat{\omega}_m$, [9].

Maes and Melkebeek propose scaling only the real parts of the eigenvalues while leaving the magnitudes of the imaginary parts unaffected [10]. This accelerates the contribution of the slower eigenvalue and thus contributes to improve the error convergence rate. The other pole, having already a large magnitude, is less amplified which gives better noise immunity.

An estimated speed signal $\hat{\omega}_m$ is required to adapt the rotor structure of the observer to the mechanical speed of the machine. The signal is derived from the current error Δi_s through a PI-controller. In fact, the term $\hat{\psi}_r \times \Delta i_s|_z$ represents the torque error ΔT_e. If a model torque error exists, the modelled speed signal $\hat{\omega}_m$ is corrected by the PI controller in Fig. 16. The phase angle of $\hat{\psi}_r$ then approximates the true field angle of the machine, and correct speed estimation is obtained.

The dynamic performance of the speed adaptation system improves if a load torque estimator is implemented. The signal flow graph Fig. 17 shows an example [10]. In addition to the speed adaptation scheme of Fig. 16, an estimate $\hat{T}_L$ of the load torque signal is used to compute the accelerating $\hat{T}_{acc}$ torque, thus forming an improved speed signal.

Different control schemes using closed loop observers are reported to operate at a minimum speed of 0.033 p.u. (50 rpm) [9], or at 0.019 p.u. (28 rpm), respectively [10].

3.2 Sliding mode observer

The effective gain of the error compensator increases when a sliding mode controller is employed for observer tuning. In contrast to the implementations previously discussed, the method proposed by *Lascu et al.* [11] completely avoids a speed adaptation scheme. Instead, the rotor equation is transformed to synchronous coordinates as shown in the signal flow graph Fig. 18. An estimated rotor field angle $\hat{\delta}$ is used for this purpose, being derived from the stator model as the argument of a first estimate $\hat{\psi}_r' = (\hat{\psi}_s - \sigma l_s i_s)/k_r$ of the rotor flux linkage vector. The rotor model then produces a second estimate $\hat{\psi}_r''$ of the rotor flux linkage vector. As field orientation is assumed, $\hat{\psi}_{rq} \approx 0$, the motion term $-j\omega_r \tau_r' \psi_r$ of the rotor model becomes obsolete. This makes the rotor model inde-

pendent of a speed or slip frequency signal. Finally, the signal $\hat{\psi}_r''$ serves to estimate the stator current vector $\hat{i}_s = (\hat{\psi}_s - k_r \hat{\psi}_r'')/\sigma l_s$.

The current error vector Δi_s is used to define the sliding hyperplane of the sliding mode compensator. The magnitude of the estimation error Δi_s is forced to the vicinity of zero by a high-frequency nonlinear switching controller. The switched complex signal is directly used to exert a compensating influence on the machine model. The robustness of the sliding mode approach ensures zero error of the estimated stator current. The complex gains $G_s(\hat{\omega}_m)$ and $G_r(\hat{\omega}_m)$ in Fig. 18 depend on the estimated angular mechanical speed $\hat{\omega}_m$, or alternatively on its reference value ω_m^* [11]. The complex gains can be even made independent of ω_m, i.e. constant, which is owed to the high effective gain of the sliding mode. With a stator resistance identification scheme included similar to the one in the lower left of Fig. 16 (discussed in Section 4.1), the authors have operated the drive system at a minimum speed of 3 rpm (0.002 p.u.) with nominal load applied.

4. PARAMETER IDENTIFICATION

The important information on the field angle and the mechanical speed is basically conveyed by the induced voltage of the stator winding, independent of the respective method that is used for sensorless control. The induced voltage $u_i = u_s - r_s i_s$ is not directly accessible by measurement. It must be estimated, either directly from the difference of the two voltage space vector terms u_s and $r_s i_s$, or indirectly when an observer is employed.

In the upper speed range above a few Hz stator frequency, the resistive voltage $r_s i_s$ is small as compared with the stator voltage u_s of the machine, and the estimation of u_i can be performed with good accuracy. Even the temperature-dependent variations of the stator resistance are negligible at higher speed. However, the small influence of r_s makes it difficult to identify this parameter at higher speed.
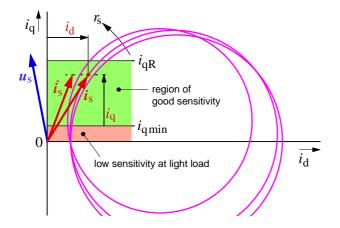
Fig. 19. Loci of the stator current vector at varying stator resistance

As the stator frequency reduces at lower speed, the stator voltage reduces almost in direct proportion, while the resistive voltage $r_s i_s$ maintains its order of magnitude. It becomes the significant term at low speed. It is particularly the stator resistance r_s that determines the estimation accuracy of the stator flux vector. A correct initial value of the stator resistance is easily identified by conducting a dc test during initialization [12]. Considerable variations of the resistance take place when the machine temperature changes at varying load. These need to be tracked to maintain the system stable at low speed.

4.1 Stator resistance identification using an observer

An observer-based parameter identification scheme utilizes the fact that the load dependent steady-state locus of the stator current vector, the *Heyland* circle, is independent of the stator frequency. However, the *Heyland* circles reduce in diameter and displace towards the imaginary axis as the stator resistance increases. An existing difference $\Delta i_s = i_s - \hat{i}_s$ between the measured and the estimated stator current vector at given nonzero load then indicates a stator resistance error. The phase displacement between i_s and $\hat{i}_s$, expressed by the internal product $i_s \circ \hat{i}_s$, is used as the error indicator; its inte-
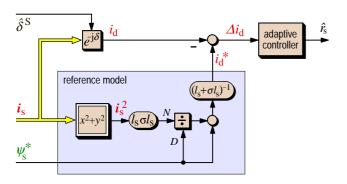

Fig. 20. Stator resistance estimation by model reference adaptive control; *N*: Numerator, *D*: Denominator

gral serves as a tuning signal that adjusts the stator resistance value until the two current vectors coincide. The signal flow structure is indicated in the lower portion of Fig. 16. The identification delay of this method is reported as 1.4 s [13].

4.2 Resistance identification by model reference adaptation

This method exploits the well defined relationship between the field oriented components of the stator current at constant flux [14]. Fig. 19 shows that, for a given value of the torque current component i_q, the field current component i_d varies as a function of r_s.

This permits defining a model reference adaptive system (MRAS) for the *d*-current component. The machine equations are derived in a stator flux oriented reference frame, hence $\boldsymbol{\psi}_s = \psi_{sd} = \psi_s$. The following equations hold [2]

$$\tau_r \frac{d\psi_s}{d\tau} + \psi_s = -\omega_r \tau_r \sigma l_s i_q + \tau_r \sigma l_s \frac{di_d}{d\tau} + l_s i_d \qquad (23a)$$

$$0 = -\omega_r \tau_r (\psi_s - \sigma l_s i_d) + \tau_r \sigma l_s \frac{di_q}{d\tau} + l_s i_q \qquad (23b)$$

where l_s is the stator inductance, and ω_r is the rotor (slip) frequency. Equations (23) simplify at steady-state, $d/d\tau = 0$,

$$\psi_s = -\omega_r \tau_r \sigma l_s i_q + l_s i_d \qquad (24a)$$

$$l_s i_q = \omega_r \tau_r (\psi_s - \sigma l_s i_d) \qquad (24b)$$

thus permitting to eliminate the rotor frequency ω_r,

$$i_d = \frac{\psi_s}{l_s + \sigma l_s} + \frac{l_s \sigma l_s}{(l_s + \sigma l_s)\psi_s} i_s^2 \overset{!}{=} i_d^* \qquad (25)$$

The result indicates that the *d*-axis current has a defined magnitude at any given excitation and load, expressed by ψ_s and i_s, provided that correct stator field orientation exists. As (25) does not depend on the stator resistance, it is used to define the value i_d^* as part of the MRAS system shown in Fig. 20. The adjustable model, by virtue of its tunable stator resistance value $\hat{r}_s$, is the drive system itself. The *d*-axis component of the measured stator current vector is determined and compared with the reference current i_d^* defined by (25). Fig. 19 shows that a deviation between the current components is due to a misalignment of r_s. Adjusting $\hat{r}_s$ can therefore serve to determine the error Δi_d in Fig. 20. A proof of convergence is given in [14]. The machine parameters l_s and σl_s as functions of the load are determined by self-commissioning [12].

The sensitivity of this identification scheme is low at light load, which is apparent from the graph Fig. 19.

4.3 Resistance identification based on reactive power

An identification algorithm that combines good no-load sensitivity and fast dynamic response relies on the orthogonal relationship in steady-state between the stator flux vector and the induced voltage [8]. The inner product of these two vectors is zero:

$$\hat{\boldsymbol{\psi}}_{\text{s}}(q) \circ \hat{\boldsymbol{u}}_{\text{i}} = \hat{\boldsymbol{\psi}}_{\text{s}}(q) \circ (\hat{\boldsymbol{u}}_{\text{s}} - \hat{r}_{\text{s}}\boldsymbol{i}_{\text{s}}) = 0 \,. \tag{26}$$

The stator flux vector in this equation must not depend on the stator resistance r_{s} to facilitate the estimation of r_{s}. An expression $\hat{\boldsymbol{\psi}}_{\text{s}}(q)$ is therefore derived from the instantaneous reactive power $q = \boldsymbol{u}_{\text{s}} \times \boldsymbol{i}_{\text{s}}|_{z}$, which notation describes the z-component of the vector product of the stator voltage and current vector.

The rotor equation in terms of $\boldsymbol{i}_{\text{s}}$ and $\boldsymbol{\psi}_{\text{s}}$ is derived in synchronous coordinates

$$\tau_{\text{sr}}' \frac{d\boldsymbol{i}_{\text{s}}}{d\tau} + \boldsymbol{i}_{\text{s}} = -\,\mathrm{j}\omega_{\text{r}}\tau_{\text{sr}}'\boldsymbol{i}_{\text{s}} + \frac{1}{r_{\text{sr}}}\left(\frac{1}{\tau_{\text{r}}} - \mathrm{j}\omega\right)\boldsymbol{\psi}_{\text{s}} + \frac{1}{r_{\text{sr}}}\boldsymbol{u}_{\text{s}} \tag{27}$$

were $\tau_{\text{sr}}' = \sigma l_{\text{s}}/r_{\text{sr}}$ and $r_{\text{sr}} = (r_{\text{s}} + l_{\text{s}}/l_{\text{r}} \cdot r_{\text{r}})$. Equation (27) is then externally multiplied by the vector $\boldsymbol{i}_{\text{s}}$, from which

$$\boldsymbol{u}_{\text{s}} \times \boldsymbol{i}_{\text{s}} - \sigma l_{\text{s}}\frac{d\boldsymbol{i}_{\text{s}}}{d\tau} \times \boldsymbol{i}_{\text{s}} \;-\mathrm{j}\omega_{\text{r}}\,\sigma l_{\text{s}}\boldsymbol{i}_{\text{s}} \times \boldsymbol{i}_{\text{s}} = $$
$$= \left(\mathrm{j}\omega - \frac{1}{\tau_{\text{r}}}\right)\boldsymbol{\psi}_{\text{s}} \times \boldsymbol{i}_{\text{s}} \tag{28}$$

is obtained. This operation eliminates the stator and the rotor resistances from (27), where these parameters form part of τ_{sr}'. Taking the z-component of all terms in (28) and assuming field orientation, $\psi_{\text{sd}} = \psi_{\text{s}}$ and $\psi_{\text{sq}} = 0$, we have

$$\hat{\psi}_{\text{s}}(q) = \frac{\left(u_{\text{q}}i_{\text{d}} - u_{\text{d}}i_{\text{q}}\right) - \omega_{\text{r}}\sigma l_{\text{s}}i_{\text{s}}^{2} + \sigma l_{\text{s}}\left(i_{\text{q}}\dfrac{di_{\text{d}}}{d\tau} - i_{\text{d}}\dfrac{di_{\text{q}}}{d\tau}\right)}{\omega\, i_{\text{d}} + \dfrac{i_{\text{q}}}{\tau_{\text{r}}}} \tag{29}$$

The stator flux value thus defined does not depend on the stator resistance.

To reduce the on-line computation time for the estimation of r_{s}, (26) is transformed to a reference frame that aligns with the stator current vector. The current reference frame (xy-frame) rotates in synchronism and is displaced with respect to stationary coordinates by the phase angle $\gamma(\tau)$ of the stator current, as shown in Fig. 21. We have $\boldsymbol{i}_{\text{s}}^{(\text{C})} = \boldsymbol{i}_{\text{s}}^{(\text{S})}\cdot\exp(-\mathrm{j}\gamma)$ and consequently $i_{\text{sx}} = i_{\text{s}}$ and $i_{\text{sy}} = 0$. Of the superscripts, $^{(\text{S})}$ refers to stator coordinates and $^{(\text{C})}$ refers to current coordinates.

The estimated value of the stator resistance is obtained as the solution of (26) in current coordinates
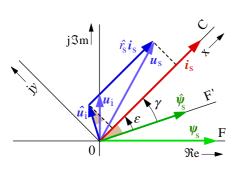

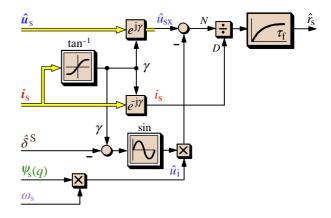Fig. 21. Vector diagram illustrating the estimation of the stator resistance; F: stator field coordinates, F': estimated stator field coordinates, C: current coordinates (x,y),

Fig. 22. Stator resistance estimator based on reactive power

$$\hat{r}_{\text{s}} = \frac{\hat{u}_{\text{sx}} - \dfrac{\hat{\psi}_{\text{sy}}}{\hat{\psi}_{\text{sx}}}\hat{u}_{\text{sy}}}{i_{\text{sx}}} = \frac{\hat{u}_{\text{sx}} - \omega_{\text{s}}\hat{\psi}_{\text{s}}(q)\,sin\left(\gamma - \hat{\delta}\right)}{i_{\text{s}}} \tag{30}$$

using the geometrical relationships

$$\frac{\hat{\psi}_{\text{sy}}}{\hat{\psi}_{\text{sx}}} = tan\left(\gamma - \hat{\delta}\right) \tag{31}$$

and

$$u_{\text{sy}} = \hat{u}_{\text{i}}\,cos\left(\gamma - \hat{\delta}\right), \tag{32}$$

which can be taken from the vector diagram Fig 21. We have furthermore in a steady-state

$$\hat{u}_{\text{i}} = \omega_{\text{s}}\,\hat{\psi}_{\text{s}}(q)\,. \tag{33}$$

The signal flow graph of the identification scheme is shown in Fig. 22. The estimated stator resistance value from (30) is passed through a low-pass filter. The filter time constant $T_{\text{f}} = \tau_{\text{f}}/\omega_{\text{sR}}$ is about 100 ms.
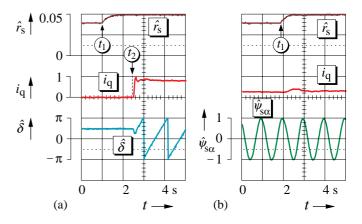

Fig. 23. Step change of the stator resistance; (a) at noload and zero stator frequency with subsequent nominal torque step, (b) at 30% rated load
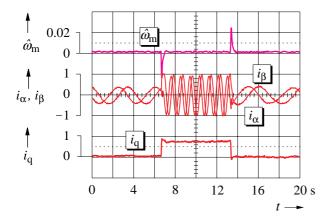
Fig. 24. Constant speed operation at 5 rpm ($\omega_\mathrm{m} = 0.003$), with load step changes of rated magnitude applied

Fig. 26. Persistent operation at zero speed; a step response proves that correct field orientation still exists after five minutes

The oscillogram Fig. 23(a) shows the response to a step increase of the stator resistances to 125% of their nominal values, applied at $t = t_1$ at no-load and zero stator frequency. The new value is identified after 250 ms. A nominal torque load step is subsequently applied at $t = t_2$, producing a fast and well damped response. This indicates that the correct resistance value was identified. Note that fast identification is important as the stator resistance may change while operating for an extended time interval at higher speed. Such changes are difficult to track as the resistive voltage is then a very small fraction of the stator voltage; only when the speed reduces can r_s be identified. An erroneous value must then be immediately corrected.

Fig. 23(b) shows the response to a step change of the stator resistances, applied at $t = t_1$, while operating at very low speed, $\omega = 0.01 \cong 0.5$ Hz, and 30% rated load. The estimated field angle is in error as long as $\hat{r}_\mathrm{s}$ adjusts to its new value, as indicated by the temporary increase of i_q.
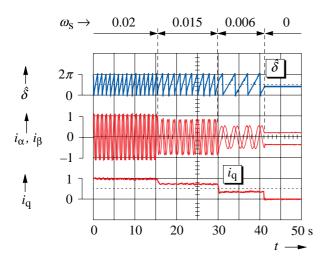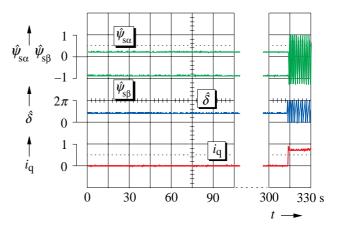
5. PERFORMANCE OF MODEL BASED CONTROL

The following oscillograms taken from an 11-kW experimental drive system demonstrate the low speed performance of sensorless speed control using the inverter model Fig. 10 and the stator flux estimation scheme Fig. 11. Very low speed operation at $\omega_\mathrm{m} = 0.003$ (5 rpm) is shown in Fig. 24. The dynamic performance is tested by repetitive torque step changes of nominal amplitude. The transient speed excursions are confined to around 2% of nominal speed. The recording Fig. 25 illustrates closed loop control at zero speed reference. The load torque is reduced in steps from 120% nominal to zero load. The respective values of stator frequency are indicated at the top of the graph. Steady-state operation at zero stator frequency is reached when the load torque has reduced to zero. Fig. 26 demonstrates that zero stator frequency operation can be maintained for a longer period of time. It is obvious that the estimation of offset drift must be suspended at zero stator frequency since a dc offset cannot be distinguished from the dc fundamental variables. Instability must be therefore expected should the dc offset change. Ongoing research aims at improving the low-speed stability at regeneration.

6. SENSORLESS CONTROL THROUGH SIGNAL INJECTION

Signal injection methods exploit machine properties that are not reproduced by the fundamental machine model described in Sections 2 and 3. The injected signals excite the machine at a much higher frequency than the fundamental. The resulting high-frequency currents generate flux linkages that close through the leakage paths in the stator and the rotor, leaving the mutual flux linkage with the fundamental wave almost unaffected. The high-frequency effects can be therefore considered superimposed to, and independent of, the fundamental behavior of the machine. High-frequency signal injection is used to detect anisotropic properties of the machine.

6.1 Anisotropies of an induction machine

A magnetic anisotropy can be caused by saturation of the

Fig. 25. Closed loop control at zero speed reference; the load torque reduces in steps from 120% nominal to zero
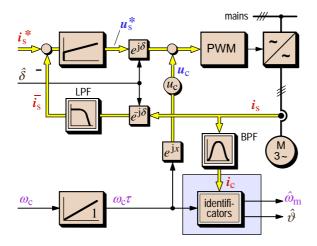
Fig. 27. Current control system and signal injection for the identification of anisotropies by means of an injected carrier

leakage paths through the fundamental field. The spatial orientation of the anisotropy is then correlated with the field angle δ, which quantity can be identified by processing the response of the machine to the injected signal. Other anisotropic structures are the discrete rotor bars in a cage rotor. Different from that, a rotor may be custom designed so as to exhibit periodic variations within a fundamental pole pitch of local magnetic or electrical characteristics. Examples are variations of the widths of the rotor slot openings [15], of the depths at which the rotor bars are buried below the rotor surface, or of the resistance of the outer conductors in a double cage, or deep bar rotor [16]. Detecting such anisotropy serves to identify the rotor position angle, the changes of which are used to obtain the shaft speed.

Anisotropic conditions justify the definition of a coordinate system that aligns with a particular anisotropy. Considering the case of saturation induced anisotropy, the maximum flux density occurs in the d-axis of a field oriented coordinate system. The fundamental field saturates the stator and rotor iron in the d-region, there producing higher magnetic resistivity of the local leakage paths. The stator and rotor currents in the conductors around the saturated d-region excite leakage fluxes having a dominating q-component. The total leakage inductance component $l_{\sigma q}$ then reduces, while the component $l_{\sigma d}$ of the unsaturated q-region remains unaffected. Such conditions lead to $l_{\sigma q} < l_{\sigma d}$ in a saturated machine.

A more general definition of an anisotropy-related reference frame locates the d-axis at that location of the airgap circumference that exhibits the maximum high-frequency time constant. This associates the d-axis with the maximum total leakage inductance, or with the minimum resistivity of conductors on the rotor surface.

There is generally more than one anisotropy present in an induction motor. The existing anisotropies have different spatial orientations such as the actual angular position of the fundamental field, the position of the rotor bars within a rotor

bar pitch, and, if applicable, the angular position within a fundamental pole pair of a custom designed rotor. The response to an injected high-frequency signal necessarily reflects all anisotropies, field-dependent and position-dependent. While intending to extract information on one particular anisotropy, the other anisotropies act as disturbances.

6.2 Signal injection

The injected signals may be periodic, creating either a high-frequency revolving field, or an alternating field in a specific, predetermined spatial direction. Such signals can be referred to as carriers, being periodic at the carrier frequency with respect to space, or time. The carrier signals, mostly created by additional components of the stator voltages, get modulated by the actual orientations in space of the machine anisotropies. The carrier frequency components are subsequently extracted from the machine current waveforms. They are demodulated and processed to retrieve the desired information.

Instead of injecting a periodic carrier, the high-frequency content of the switched waveforms in a PWM controlled drive system can be exploited for the same purpose. The switching of the inverter produces a repetitive excitation of the high-frequency leakage fields. Their distribution in space is governed by the anisotropies of the machine. Measuring and processing of adequate voltage or current signals permits identifying their spatial orientations.

6.3 Injection of a revolving carrier

A polyphase carrier rotating at frequency ω_c can be generated by the voltage space vector

$$\boldsymbol{u}_c = u_c \cdot e^{j\omega_c \tau}, \tag{34}$$

which is added to the controlling voltage of the pulsewidth modulator as shown in Fig. 27. The interaction with the machine anisotropies produces a space vector $\boldsymbol{i}_c$ of carrier frequency ω_c, appearing as a component of the measured stator current vector $\boldsymbol{i}_s$. It is separated by a band-pass filter BPF from the fundamental current $\boldsymbol{i}_{s1}$ of lower frequency, and from the switching harmonics of higher frequencies.
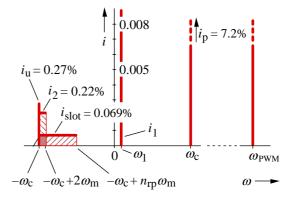

Fig. 28. Amplitudes of the spectral components from [15]

A single anisotropy having one spatial cycle per pole pitch is typical for saturation effects, or for a custom designed machine. Such anisotropy is characterized by a total leakage inductance tensor

$$\boldsymbol{l}_\sigma{}^{(X)} = \begin{bmatrix} l_{\sigma d} & 0 \\ 0 & l_{\sigma q} \end{bmatrix} \qquad (35)$$

being defined in an *xy*-coordinate system $^{(X)}$ that rotates at ω_x in synchronism with the anisotropy under consideration. The *x*-axis coincides with the region of the highest transient leakage inductance. This is the field axis of a saturated machine, when $\omega_x = \omega_s$, or the real axis of a custom designed rotor, when $\omega_x = \omega_m$.

To compute the response of the machine to carrier excitation, (34) is multiplied by $exp(-j\omega_x)$, which transforms this equation to *xy*-coordinates. The high-frequency components are then described by the differential equation

$$\boldsymbol{u}_c{}^{(X)} = u_c \cdot e^{j(\omega_c - \omega_x)\tau} = \boldsymbol{l}_\sigma{}^{(X)} \frac{d\boldsymbol{i}_c{}^{(X)}}{d\tau} \qquad (36)$$

which is solved for $\boldsymbol{i}_c$. Considering $\omega_c \gg \omega_x$ leads to the solution

$$\boldsymbol{i}_c{}^{(X)} = \frac{-ju_c}{2\omega_c\, l_{\sigma d}\, l_{\sigma q}} \begin{bmatrix} (l_{\sigma d} + l_{\sigma q})e^{+j(\omega_c - \omega_x)\tau} \\ +(l_{\sigma d} - l_{\sigma q})e^{-j(\omega_c - \omega_x)\tau} \end{bmatrix}, \qquad (37)$$

which is subsequently transformed back to the stationary reference frame

$$\boldsymbol{i}_c{}^{(S)} = \frac{-ju_c}{2\omega_c\, l_{\sigma d}\, l_{\sigma q}}$$

$$\left[(l_{\sigma d} + l_{\sigma q})e^{j\omega_c\tau} + (l_{\sigma d} - l_{\sigma q})e^{j(-\omega_c + 2\omega_x)\tau} \right] \qquad (38)$$

$$= \boldsymbol{i}_p + \boldsymbol{i}_n$$

The result shows the existence of a first current space vector $\boldsymbol{i}_p$, rotating at carrier frequency ω_c in a positive direction, and second space vector $\boldsymbol{i}_n$ that rotates at the angular velocity $-\omega_c + 2\omega_x$, i.e. in a negative direction. The latter component conserves the angular orientation $\omega_x\tau$ of the particular anisotropy.

Fig. 28 shows an example of the respective current amplitudes, obtained using a 250-Hz revolving carrier of 15% dc bus amplitude. The induction motor under test has its rotor slot openings modifed in a sinusoidal pattern with a maximum to minimum slot width ratio of 5, [15].

The spectral components are referred to the nominal machine current I_R. A negative sequence component $i_2 = 0.22\%$ is saturation induced, while $i_u = 0.27\%$ results from unsymmetrical signal acquisition gains, and $i_{slot} = 0.069\%$ is the component of the rotor slot anisotropy. Such small signals call for special efforts to ensure that the low signal levels are sufficiently reproduced when doing the analog-to-digital conversion of the measured currents [17]. The same paper [17] proposes a particular stator current observer to alleviate the loss of control bandwith caused by the lowpass filter in Fig. 27.

The shaded areas in Fig. 28 mark the frequency spread when the rotor speed varies between 0 and 0.1 p.u. The figures underline the general difficulties of revolving carrier injection methods: (i) the extreme low signal-to-noise ratio, which is around 10^{-3} in the example of Fig. 28, and (ii) the poor spectral separation between the useful signal i_{slot}, and the disturbances i_u and i_2, as exemplified in Fig. 28.

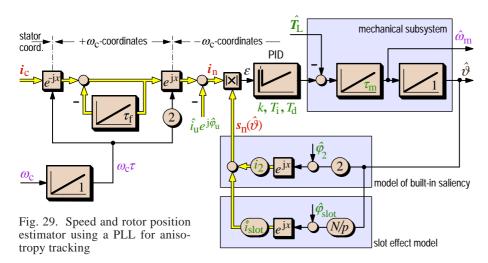Rotating at the frequency of the carrier signal, the trajectory (38) of the current vector $\boldsymbol{i}_c$ follows in fact an elliptic path. The axis ratio of the ellipse is $l_{\sigma q}/l_{\sigma d}$, a close to unity value that ranges between 0.9 and 0.96 [15, 18]. It is therefore difficult to identify the angular inclination of the ellipse and thus determine the angular orientation of the anisotropy. A direct extraction is problematic, as the characterizing components in $\boldsymbol{i}_n$ are very small, being superimposed by the larger positive sequence current vector $\boldsymbol{i}_p$, and contaminated by the effect of other anisotropies and disturbances. Finally, all these signals are buried under the much larger fundamental current i_{s1}, and under the switching harmonics [18].

6.4 Estimation based on an injected revolving carrier

Degner and *Lorenz* [15] use a dynamic model of the mechanical subsystem of the drive motor to enable spectral separation. The machine rotor has a custom designed anisotropy of one pole pair periodicity. The carrier frequency is 250 Hz.

A signal flow graph of the speed and rotor position estimator is shown in Fig. 29. The input signal is the carrier dependent space vector $\boldsymbol{i}_c$, extracted by

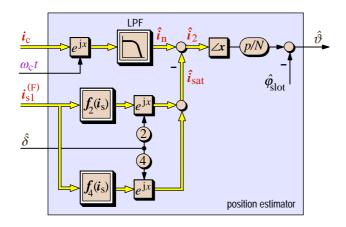Fig. 29. Speed and rotor position estimator using a PLL for anisotropy tracking

Fig. 30. Modelling and compensation of the saturation induced anisotropy for a position estimation scheme based on the rotor slot anisotropy

Fig. 32. Components of the compensation profile i_f in one particular operating point, characterized by the respective values i_d and i_q

the band-pass filter in Fig. 27. It is first transformed to a $+\omega_c$-reference frame in which i_p from (38) appears as a complex constant. Its contribution is nullified through the feedback action of an integrator. The remaining signal i_n contains all negative sequence components. It is transformed to a $-\omega_c$-reference frame. This transformation shifts the frequency origin in Fig. 28 to $-\omega_c$. The unbalance disturbance, now at frequency zero, is compensated by an estimated vector $\hat{i}_u = i_u \, exp(j\hat{\varphi}_u)$. The negative sequence components i_n convert to positive sequence signals of frequencies $2\omega_m$ and $n_{rp}\omega_m$, where n_{rp} is the number of rotor slots per pole pair.

Using two anisotropy models in Fig. 29, a synchronization signal

$$s_n(\hat{\vartheta}) = \hat{i}_2 \, e^{j(2\hat{\vartheta}+\hat{\varphi}_2)} + \hat{i}_{slot} \, e^{j(n_{rp}\hat{\vartheta}+\hat{\varphi}_{slot})}. \tag{39}$$

is generated as a function of an estimated position angle $\hat{\vartheta}$, being obtained from a model of the mechanical subsystem of the drive. The model is shown in the upper right of Fig. 29. The signal $s_n(\hat{\vartheta})$ is phase-locked with the transformed nega-
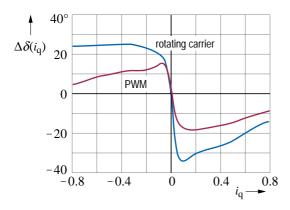

Fig. 31. Phase displacement $\Delta\delta(i_q)$ between the identified orientation and the field axis for different types of transient excitation
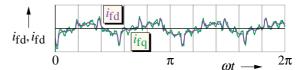
tive sequence current i_n. Both signals contain the same frequencies since $\vartheta = \int\omega_m d\tau$. The phase displacement $\hat{\varphi}_2$ in (39) compensates signal filtering delays, and $\hat{\varphi}_{slot}$, in addition, reflects the displacement between the two anisotropies of the machine.

While the error signal $\varepsilon = i_n \times s_n(\hat{\vartheta})|_z$ is close to zero in a steady-state, it becomes nonzero at any transient condition. It is fed to a PID controller which synthesizes an acceleration torque signal to act on the model of the mechanical subsystem. A feedforward signal $\hat{T}_L$ representing the load torque improves the estimation dynamics. It is obtained from a separate load model.

The saturation induced anisotropy, rotating at ω_s, is not modelled in this approach, which limits its application to unsaturated machines. Saturation and custom designed anisotropies are difficult to separate since $\omega_s \approx \omega_m$.

For this reason, *Teske and Asher* rely on the rotor slot anisotropy for position estimation [19] while compensating the saturation effects. A saturation model of the machine is used to generate excitation and load dependent compensation signals, so as to suppress the saturation induced disturbances. The proposed structure is shown in Fig. 30. The carrier frequency components i_c obtained from the system Fig. 27 are transformed to $-\omega_c$-coordinates. Subsequent low-pass filtering yields the space vector $\hat{i}_n$ that comprises all negative sequence components: $\hat{i}_{slot}$, $\hat{i}_{sat}$ and also i_u.

An estimation of the disturbance vector $\hat{i}_{sat}$ is needed to attenuate the saturation induced effects The vector $\hat{i}_{sat}$ is modelled by the complex functions $f_2(i_{s1})$ and $f_4(i_{s1})$, where $f_2(i_{s1})$ generates the second spatial harmonic component, and $f_4(i_{s1})$ the fourth harmonic, both referred to the fundamental field. Modelling higher harmonic components may be required, depending on the properties of a particular machine. The input signal of the complex functions is the fundamental stator current $i_{s1}^{(F)}$ in field coordinates. Its i_d-component characterizes the mutual flux, and the i_q-component the load. Both components control the saturation of the machine. The total disturbance vector $\hat{i}_{sat}$ is synthesized as the sum of its harmonic components, these being adjusted to their respective phase displacements according to the actual angular position $\hat{\delta}$ of the revolving fundamental field in the machine. The respective functions $f_2(i_{s1})$ and $f_4(i_{s1})$ for a particular machine are determined in an off-line identification process [19].

In addition to the saturation through the magnetizing field, a load current dependent phase displacement $\Delta\delta(i_q)$ exists
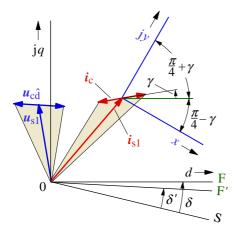
Fig. 33. Vector diagram showing the injected ac carrier i_c in different reference frames; i_{s1}: fundamental current, F: field oriented frame, F': estimated field oriented frame, S: stationary frame

$$\hat{\boldsymbol{i}}_{\text{slot}} = \hat{i}_{\text{slot}} e^{j\left(\frac{N}{p}\hat{\vartheta} + \hat{\varphi}_{\text{slot}}\right)}. \qquad (40)$$

is not much distorted. This could permit replacing the complex and parameter dependent PLL structure in Fig. 29 by the simple calculation of the phase angle of $\hat{\boldsymbol{i}}_{\text{slot}}$ from (40) as illustrated in Fig. 30, [24]. However, to obtain a speed signal, the rotor position signal must be differentiated. This amplifies its residual noise, for which reason the PLL approach appears preferable [25].

Current publications on revolving carrier methods show that numerous side effects require the signal processing structures to get more and more involved, while the dependence on parameters or on specific off-line commissioning procedures persists.

Consoli *et al.* propose a different approach which is described in [26] as modulating the saturation level of the airgap field by a high-frequency revolving carrier. As high-frequency fields tend to develop in the leakage paths, the leakage inductances being affected by the main field through saturation, an unbalance of the phase leakage voltages carries the information of the field angle. The unbalance of the leakage voltages reflects in the zero sequence component of the stator voltages. This quantity is measured as the voltage difference between the midpoint of the dc link and either the neutral of the stator winding in wye connection, or the voltage potential of an artificial neutral formed by resistors.

The carrier frequency is variable and chosen as

$$\omega_c = \omega_o + \omega_s \qquad (41)$$

where ω_s is the stator frequency and $\omega_o \approx 2\pi \cdot 500/\text{s}$ is constant [26]. Hence, according to (41), the zero sequence voltage maintains the constant frequency $\omega_c - \omega_s$. It is sampled at four times the carrier frequency to ensure that its respective maximum, minimum and zero values coincide with the sampling instants. Deviations serve to control the carrier frequency by adjusting ω_s in (41). Integrating ω_s finally yields the field angle.

The flux linkage magnitude is then determined from the magnitude of the zero sequence voltage using a precalibrated

between the identified orientation and the field axis. According to *Caruana* [20], this displacement depends in the type of transient excitation. The curves in Fig. 31 illustrate the effect. The comparatively low frequency of a revolving carrier gives more sensitivity to the torque current i_q than the high-frequency components of PWM waveforms (see Section 6.6). The effect is owed to different penetration depths into the rotor surface of the transient fields [21]. There is also a displacement at no-load since the saturation anisotropy does not align with neither the stator field not the rotor field.

Another problem is the nonlinearity of the PWM inverter which causes distortions of the machine currents. These generate additional negative sequence current components that tend to fail the operation of the position estimator [22]. In addition, the high-frequency carrier currents force the stator currents to multiple zero crossings when the fundamental phase currents are close to zero. The effect, illustrated in Fig. 14, causes disturbances that established methods for dead-time compensation [6, 23] cannot handle.

Being time-discrete events, the current distortions are difficult to compensate in a frequency domain method. A fairly involved off-line identification method was proposed by *Teske and Asher* [22] which generates sets of time-variable profiles over one electrical revolution, one specific profile for every operating point in terms of load and excitation level. The profiles model the nonlinearity effect caused by the high-frequency carrier signals of a particular inverter. An example is shown in Fig. 32. Such waveforms are defined in an off-line identification process and retrieved on-line to reconstruct the particular vector $\hat{\boldsymbol{i}}_{\text{inv}}$ that fits the actual operating point [24].

If the compensation of saturation effects, inverter nonlinearity and signal unbalance, represented by the respective vectors $\hat{\boldsymbol{i}}_{\text{sat}}$, $\hat{\boldsymbol{i}}_{\text{inv}}$ and $\hat{\boldsymbol{i}}_u$, is performed with sufficient accuracy, the remaining signal
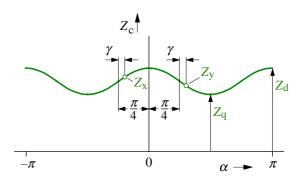

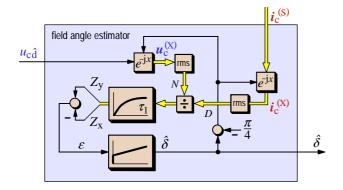Fig. 34. Impedance at carrier frequency vs. the circumferential angle α in field coordinates; γ: error angle

Fig. 35. Signal flow graph of a field angle estimation scheme based on impedance measurements in quadrature axes
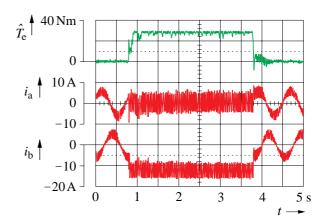

Fig. 36. Torque controlled operation showing the dynamic performance and demonstrating persistent operation at zero stator frequency at 150% of rated torque; reproduced from [27]

saturation table. Also the stator currents can be estimated from available state variables, which then eliminates the current sensors. The method is demonstrated to work well throughout the low-frequency range [26].

6.5 Injection of an alternating carrier

Revolving carriers scan the whole circumferential profile of anisotropies that exist in a machine. The objective is to determine the characteristics of a particular anisotropy with a view to subsequently identifying its spatial orientation. An alternative class of methods relies on injecting not a rotating, but alternating carrier in a specific, though time-variable spatial direction. The direction is selected in an educated guess to achieve maximum sensitivity in locating the targeted anisotropy. Use is made of already existing knowledge, which is updated by acquiring only an incremental error per sampling period.

6.5.1 Balance of quadrature impedances

The approach of *Ha and Sul* [27] aims at identifying a field angle while the machine operates at low or zero speed. The principle is explained with reference to Fig. 33. The diagram shows the field oriented coordinate system F, which appears displaced by the field angle δ as seen from the stationary reference frame S. A high-frequency ac carrier signal of amplitude u_c is added to the control input of the pulsewidth modulator, written in field coordinates

$$\boldsymbol{u}_s^{*(F)} = \left(u_d + u_c \cos \omega_c t\right) + j u_q \tag{42}$$

The time-variable voltage vector $u_{c\hat{d}} = u_c \cos \omega_c \tau$ is shown in the left of Fig. 33. The signal excites the machine in the direction of the estimated *d*-axis. This direction may have an angular displacement $\hat{\delta} - \delta$ from the true *d*-axis, the location of which is approximately known from the identification in a previous cycle.

The injected voltage (42) adds an ac component $\boldsymbol{i}_c$ to the regular stator currents of the machine, represented in Fig. 33 by the space vector $\boldsymbol{i}_{s1}$ of the fundamental component. Ow-

ing to the anisotropic machine impedance, the high-frequency current $\boldsymbol{i}_c$ develops at a spatial displacement γ with respect to the true field axis of the machine, and at $\gamma + (\delta - \hat{\delta})$ with respect to the injected voltage.

When the machine is operated in saturated conditions, its impedance Z_c at carrier frequency ω_c is a function of the circumferential angle α in field coordinates, as schematically shown in Fig. 34. The impedance has a maximum value Z_d in the *d*-axis, and a minimum value Z_q in the *q*-axis. Note that Z_c depends on the *total* leakage inductance, which makes the estimated field angle $\hat{\delta}$ represent neither the stator field angle, nor the rotor field angle. The fact carries importance when designing the field oriented control.

The identification of the *d*-axis is based the assumption of a symmetric characteristic $Z_c(+\alpha) = Z_c(-\alpha)$. An orthogonal *xy*-coordinate system is introduced in Fig. 33, having its real axis displaced by $-\pi/4$ with respect to the estimated *d*-axis. Its displacement with the true *d*-axis is then $-(\pi/4 - \gamma)$.

The identification procedure is illustrated in the signal flow graph Fig. 35. The band-pass-filtered current $\boldsymbol{i}_c$ from Fig. 27 and also the excitation signal $u_{c\hat{d}}$ are transformed to *xy*-coordinates and then converted to complex vectors having the respective rms amplitudes and conserving the phase angles. From these, the complex high-frequency impedance

$$\boldsymbol{Z}_c^{(X)} = Z_x + j Z_y = \frac{\boldsymbol{u}_c^{(X)}}{\boldsymbol{i}_c^{(X)}} \tag{43}$$

is formed which is a function of the transformation angle $\hat{\delta} - \pi/4$; as seen from the field oriented coordinate system in Fig. 33, the transformation angle is $-(\pi/4 - \gamma)$. Fig. 34 shows that the real and imaginary components in (43), Z_x and Z_y, respectively, would equal if accurate field alignment, $\gamma = 0$, existed. A positive error angle γ makes Z_x increase, and Z_y decrease. Hence an error signal
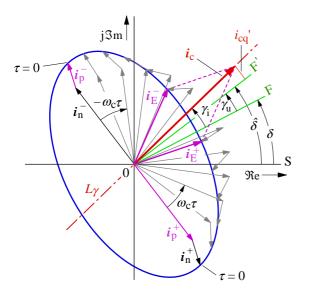
$$\varepsilon = Z_y(\gamma) - Z_x(\gamma) \tag{44}$$

Fig. 37. The elliptic trajectories and i_E^+ and i_E^-, created by four circular rotating space vectors; S: stationary coordinates , F: field coordinates, F´: estimated field coordinates

can be constructed which adjusts the estimated field angle $\hat{\delta}$ to an improved value using a PI controller. Fig. 35 shows that this angle is used for coordinate transformation. In a condition of accurate field alignment, $\hat{\delta} \to \delta$, from which $\gamma \to 0$ follows.

Measured characteristics from a 3.8-kW induction motor show that the difference between the impedance values Z_d and Z_q is small when the machine is fully saturated [27]. This reduces the error sensitivity and thus requires carrier injection at high amplitude. The curves in [27] also show that the symmetry of $Z_c(\alpha)$ may not be guaranteed for every motor. An asymmetric characteristic would lead to estimation errors.

The oscillogram Fig. 36 demonstrates that closed loop torque control at zero stator frequency and 150% rated load is achieved, although the dynamic performance is not optimal [27]. Also noticeable is the very high amplitude of the high-frequency current when the load is applied. It is therefore preferred restricting the use of an injected carrier only to low speed values, as demonstrated in a practical application [28].

6.5.2 Evaluation of elliptic current trajectories

The carrier injection methods so far described suffer from certain drawbacks. We have the poor signal-to-noise ratio and the parameter dependence of the revolving carrier methods, and the low sensitivity of the quadrature impedance method.

Linke et al. [29] propose the estimation of anisotropy characteristics based on an interpretation of the elliptic current trajectories that are generated by an alternating carrier signal. The ac carrier voltage of this method is injected at an estimated displacement angle $\hat{\delta}$, where $\hat{\delta}$ deviates from the true

field angle δ by an error angle γ_u, and hence

$$\hat{\delta} = \delta + \gamma_u \qquad (45)$$

The carrier voltage in stationary coordinates is

$$\boldsymbol{u}_c^{(S)} = u_c \cos \omega_c \tau \cdot e^{j\hat{\delta}} \qquad (46)$$

A transformation to field coordinates is done by multiplying (46) by $\exp(-j\delta)$. Referring to (36) yields the differential equation

$$\boldsymbol{u}_c^{(F)} = u_c \cos \omega_c \tau \cdot e^{j(\hat{\delta}-\delta)} = \boldsymbol{l}_\sigma^{(F)} \frac{di_c}{d\tau}. \qquad (47)$$

The excitation at carrier frequency does not affect the fundamental machine quantities. The resulting carrier frequency current i_c is therefore only determined by the anisotropic leakage inductance (35), as indicated in the right-hand side of (47).

The solution of (47) is

$$\boldsymbol{i}_c^{(F)} = \frac{u_c}{\omega_c} \sin \omega_c \tau \cdot \left(\frac{1}{l_{\sigma d}} \cos(\hat{\delta}-\delta) + j\frac{1}{l_{\sigma q}} \sin(\hat{\delta}-\delta) \right) \quad (48)$$

The true field angle δ in this equation is the unknown variable. A multiplication by $\exp(j\delta)$ transforms (48) back to stationary coordinates. The result is $\boldsymbol{i}_c^{(S)}$.

To gain an insight in the physical nature of $\boldsymbol{i}_c^{(S)}$, the harmonic functions are expressed by equivalent complex space vectors. Referring to (45), the result can be written as

$$\boldsymbol{i}_c^{(S)} = \boldsymbol{i}_E^+ + \boldsymbol{i}_E^-, \qquad (49a)$$
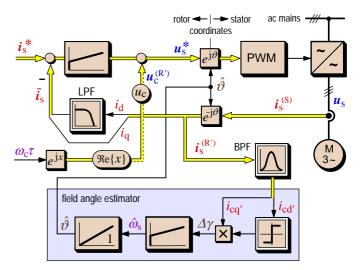
where

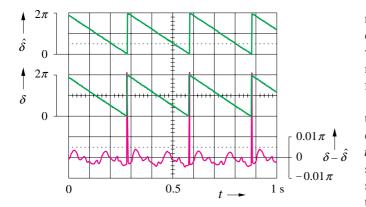Fig. 38. Signal flow graph of a field angle estimation scheme using an alternating carrier

Fig. 39. Measured signals obtained with the field angle estimation scheme in Fig. 36, operated at 0.004 ω_{sR} (6 rpm); from top: estimated field angle, estimation error, true field angle

$$i_E^+ = \frac{-ju_c}{4\omega_c\, l_{\sigma d}\, l_{\sigma q}} \left[\begin{array}{l} \left(l_{\sigma d} + l_{\sigma q}\right)e^{j(\omega_c\tau + \hat{\delta})} \\ + \left(l_{\sigma d} - l_{\sigma q}\right)e^{j(-\omega_c\tau + \hat{\delta} - 2\gamma_u)} \end{array} \right]$$

$$= i_p^+ + i_n^+ \qquad (49b)$$

describes the elliptic trajectory of a current vector that rotates in a positive direction, and

$$i_E^- = \frac{ju_c}{4\omega_c\, l_{\sigma d}\, l_{\sigma q}} \left[\begin{array}{l} \left(l_{\sigma d} + l_{\sigma q}\right)e^{j(-\omega_c\tau + \hat{\delta})} \\ + \left(l_{\sigma d} - l_{\sigma q}\right)e^{j(\omega_c\tau + \hat{\delta} - 2\gamma_u)} \end{array} \right]$$

$$= i_n^- + i_p^- \qquad (49c)$$

represents the elliptic trajectory of a negatively rotating current vector. Fig. 37 illustrates that the current components (49b) and (49c) superimpose: both elliptic trajectories are congruent. They are composed of current vectors that rotate on circular trajectories, and in opposite directions. As indicated by (49b), the elliptic trajectory i_E^+ that develops in a positive direction decomposes into a positive sequence current vector i_p^+ and a negative sequence current vector i_n^+. Similar conditions hold for the trajectory i_E^-, building up in a negative direction and being composed, according to (49c), of a positive sequence current vector i_p^- and a negative sequence current vector i_n^-.

As the true field angle δ may not be exactly known, the ac carrier voltage is injected at a spatial displacement γ_u from the true field axis, (45). The direction of the carrier voltage $\delta + \gamma_u$ coincides with the F'-axis in Fig. 37. Owing to the anisotropy of the machine, the ac carrier current i_c deviates spatially from the injected voltage. It develops in the direction $\delta + \gamma_i$, where $|\gamma_i| \geq |\gamma_u|$. This means that the elliptic trajectories of the current space vectors i_E^+ and i_E^- take their spatial orientation from the existing anisotropy, not from of the direction in which the carrier signal is injected.

The vector diagram Fig. 37 demonstrates that the geomet-

ric additions over time of all space vector components in (49) define the locus of a straight line L_γ, inclined at the angle γ_i with respect to the true field axis F. This circumstance permits identifying a misalignment of the estimated reference frame F'.

The angular displacement $\gamma_i - \gamma_u$ between the locus L_γ of the carrier current and the direction F' of carrier injection is determined by the quadrature component $i_{cq}' = \Im m\{i_c^{(F')}\}$ of i_c in the estimated reference frame F', shown in Fig. 37. The signal i_{cq}' is of alternating nature, the same as i_c. An error signal characterizing the displacement $\gamma_i - \gamma_u$ is therefore obtained by controlled rectification according to

$$\Delta\gamma \approx i_{cq}' \cdot sign(i_{cd}') \qquad (50)$$

which holds for small displacement angles $\Delta\gamma$. Fig. 38 shows the signal flow graph, [30]. The error signal $\Delta\gamma$ is fed to a PI controller. Its output is integrated to create the estimated field angle $\hat{\delta}$ in a closed loop. Since $d\delta/d\tau = \omega_s$, the integrator output equals ω_s.

As the error signal $\Delta\gamma$ gets minimized, both γ_i and γ_u tend to zero, and $\hat{\delta} \to \delta$. Field orientation is thus obtained.

The following features make this approach robust and sensitive:

- As in every carrier injection scheme, carrier demodulation must be done with reference to the injected voltage. Here, i_{cd}' is used as a reference signal; this signal has passed the inverter, the same as the error signal i_{cq}'. As both signals are subjected to the nonlinear distortions of the inverter, the disturbances compensate. The scheme does not even require dead time compensation.

- Both the positive sequence and the negative sequence carrier components, i_E^+ and i_E^-, are exploited to compose the error signal. Their sum gives a better signal-to-noise ratio.

- The dynamics of the speed and torque control system are not impaired as the carrier signal does not appear in the torque building current component i_q. Therefore, the measured q-current need not be low-pass filtered, as is required when a rotating carrier is used, Fig. 27. According to Fig. 38, such filter is only provided for the component i_d in the excitation axis.

Fig. 39 displays the measured waveforms of the true and the estimated field angles, measured at 0.067 ω_{sR}, or 100 rpm, and the estimation error, recorded from a 0.75-kW induction motor [30]. Using carrier injection, a field angle signal of good accuracy can be also obtained at zero speed, although its ripple content could be an undesired disturbance. The ripple in Fig. 39 originates from other anisotropies of the induction motor. Its disturbing influence can be eliminated by using a filtered field angle signal for parameter tuning of a fundamental machine model or observer [31].

6.6 High-frequency excitation by PWM switching
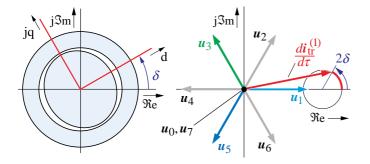
The switching of a PWM inverter subjects the machine to

Fig. 40. Anisotropic, saturated rotor causing the transient current derivative $di_{tr}/d\tau$ to deviate from the direction of the exciting switching state vector u_1
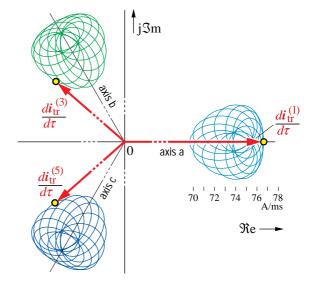

Fig. 41. Loci of the vectors $di_{tr}(\vartheta, \delta)/dt$ at transient excitation in the directions of the three phase axes, (locked rotor, origin suppressed); the superscripts indicate the the exciting switching state vectors

repetitive transient excitation. Other than the fundamental quantities, the transient flux components, owing to their high-frequency content, do not penetrate sufficiently fast through rotor surface to establish mutual flux linkages. These fluxes, instead, create only separate linkages with the respective stator and rotor windings, thus contributing to the total leakage flux. A detailed study [21] shows that the fundamental flux density wave in any given operating point and the transient leakage fields that result from an additional step-like excitation can be separately analyzed, provided a linearized magnetization curve is assumed. The total flux linkage distribution is then obtained as the superposition of the fundamental and the transient component.

In accordance with these results, the following analysis refers only to the transient leakage fields. These are represented by the space vector of the transient leakage flux linkages

$$\boldsymbol{\psi}_{\sigma tr} = \boldsymbol{l}_{\sigma} \boldsymbol{i}_{tr} \qquad (51)$$

where $\boldsymbol{i}_{tr}$ is the current component produced by a voltage transient $\boldsymbol{u}_{tr}$, and $\boldsymbol{l}_{\sigma}$ is the tensor of the total leakage inductance (35). The stator resistance is neglected. In the event of an inverter commutation, the transient stator voltage component

$$\boldsymbol{u}_{tr} = \boldsymbol{u}_{s} - \boldsymbol{u}_{s1} \qquad (52)$$

produces a change of the leakage flux vector

$$\frac{d\boldsymbol{\psi}_{\sigma tr}}{d\tau} = \boldsymbol{l}_{\sigma}\frac{d\boldsymbol{i}_{tr}}{d\tau} + \boldsymbol{i}_{tr}\frac{d\boldsymbol{l}_{\sigma}}{d\tau} = \boldsymbol{u}_{tr} \qquad (53)$$

which adds to the fundamental component $\boldsymbol{\psi}_{\sigma 1}$. In (52), $\boldsymbol{u}_{s1}$ is the fundamental stator voltage associated to an assumed steady-state condition that prevailed before the commutation.

The following conditions are introduced to simplify the mathematical analysis of the anisotropies:

• Of the product $\boldsymbol{l}_{\sigma}d\boldsymbol{i}_{tr}(\vartheta, \delta)/d\tau$ in (53), only the components in the direction of the phase axes will be computed. The characteristic quantities are then scalar inductance components $l_{\sigma a}$, $l_{\sigma b}$, and $l_{\sigma c}$ of the respective phase axes.

• Accurate position estimation is only required at very low speed. Changes with time of the inductance tensor are then small which permits neglecting the term $\boldsymbol{i}_{tr}d\boldsymbol{l}_{\sigma}/d\tau$ in (53).

The conventional model of the induction motor assumes the leakage inductances of the three phases as balanced. This balance is disturbed in the presence of machine anisotropies, giving rise to different leakage inductance values in the respective phases. The space vector $\boldsymbol{u}_{tr}$ of the transient voltage component then produces an excursion of the vector $\boldsymbol{i}_{tr}$ in a spatial direction that differs from that of the vector $\boldsymbol{u}_{tr}$. This phenomenon requires representing the leakage inductance in (51) and (53) by the tensor $\boldsymbol{l}_{\sigma}$ instead of the customary scalar coefficient l_{σ}.

To study the effect, a homogeneous rotor, but saturated in a fixed angular position δ, is considered as shown in Fig. 40. A transient current $\boldsymbol{i}_{tr}^{(1)}$ results from the turn-on of the switching state vector $\boldsymbol{u}_1$. Since $r_s = 0$, also $\boldsymbol{u}_{s1} = 0$ in (52) and $d\boldsymbol{l}_{\sigma}/d\tau = 0$ since δ is constant. Then, multiplying (53) by the inverse

$$\boldsymbol{l}_{\sigma}^{-1\,(S)} = \frac{1}{l_{\sigma d}\,l_{\sigma q}} \cdot \qquad (54)$$

$$\begin{bmatrix} \frac{1}{2}\left(l_{\sigma d} + l_{\sigma q}\right) - \frac{1}{2}\left(l_{\sigma d} - l_{\sigma q}\right)cos\,2\delta & \frac{1}{2}\left(l_{\sigma d} - l_{\sigma q}\right)sin\,2\delta \\ \frac{1}{2}\left(l_{\sigma d} - l_{\sigma q}\right)sin\,2\delta & \frac{1}{2}\left(l_{\sigma d} + l_{\sigma q}\right) + \frac{1}{2}\left(l_{\sigma d} - l_{\sigma q}\right)cos\,2\delta \end{bmatrix}$$

of the leakage inductance tensor yields

$$\frac{d\boldsymbol{i}_{tr}^{(1)}}{d\tau} = \frac{1}{2}\left[\left(l_{\sigma d} + l_{\sigma q}\right) - \left(l_{\sigma d} - l_{\sigma q}\right)cos\,2\delta + j\left(l_{\sigma d} - l_{\sigma q}\right)sin\,2\delta\right]\boldsymbol{u}_1 \qquad (55)$$

Assuming various different values of δ, (55) demonstrates

that the derivative vector $di_{tr}^{(1)}/d\tau$ is located on a circle that is centered on the axis of the exciting vector u_1. The vector displaces on the circle circumference by 2δ as the saturation displaces by δ, Fig. 40.

An induction motor with open rotor slots exhibits an additional anisotropy of $n_{rp} \cdot \vartheta$ periodicity, where ϑ is the rotor position angle and n_{rp} is the number of rotor slots per pole pair. The effects of saturation and rotor slot anisotropy then superimpose. The resulting derivative vector $di_{tr}^{(1)}(\vartheta, \delta)/d\tau$ locates on one point of the epicyclic curve centered on the real axis in Fig. 41. The spatial high-frequency component of this curve is caused by the rotor anisotropy; it displaces by $n_{rp} \cdot \vartheta$ around the center point of the circle in Fig. 40. The low-frequency component is due to magnetic saturation; it displaces by 2δ.

In a loaded machine, the angular velocities $d\vartheta/d\tau$ and $d\delta/d\tau$ differ by the slip velocity. The asynchronism causes the patterns in Fig. 41 to change as time elapses, while they maintain their typical characteristics.

A transient excitation in the direction of the switching state vector u_3 produces a different derivative vector $di_{tr}^{(3)}(\vartheta, \delta)/d\tau$. This vector points to a location on the epicyclic pattern centered on the b-axis in Fig. 41. Finally, an excitation in the direction of u_5 gives rise to a vector $di_{tr}^{(5)}(\vartheta, \delta)/d\tau|_c$ which targets the pattern centered on the c-axis.

All three discrete derivative vectors shown in Fig. 41 refer to a given constant rotor position ϑ and constant spatial orientation δ of the saturation. Even though, the derivative vectors point to different locations on the respective patterns since the number of rotor slots per pole pair is not a multiple of three. This is true for most induction machines. On this condition, the rotor slot patterns, as seen from the respective phase axes, appear displaced by 0, 1/3, or 2/3 slot pitch, respectively [18].

6.6.1 The Inform method

The response of an anisotropic machine to PWM transients can be exploited for field angle estimation at very low speed and also at zero stator frequency. *Schroedl* [32] calls his approach the *INFORM* method (indirect flux detection by on-line reactance measurement). The analysis starts from the stator voltage equation in stator coordinates

$$u_s^{(S)} = r_\sigma i_s + l_\sigma^{(S)} \frac{di_s}{d\tau} + \frac{k_r}{\tau_r}(j\omega_m \tau_r - 1)\psi_r \quad (56)$$

where the tensor $l_\sigma^{(S)}$ models the saturation induced anisotropy. The rate of change $\Delta i_s/\Delta\tau$ of the stator current vector is measured as a difference Δi_s over a short time interval $\Delta\tau$, while a constant switching state vector is applied as u_s. The influence on Δi_s of the resistive voltage $r_s i_s$ and the back emf is eliminated by taking two consecutive measurements while applying two switching state vectors in opposite directions, e. g. u_1 and $u_4 = -u_1$ in Fig. 40, each for a time interval $\Delta\tau$. It can be assumed that the fundamental components of i_s and ψ_s do not change between two measurements.

Inserting the two switching state vectors u_1 and u_4 separately in (56) and taking the difference of the two resulting equations yields

$$u_1 - u_4 = l_\sigma \left(\frac{\Delta i_s^{(u_1)}}{\Delta\tau} - \frac{\Delta i_s^{(u_4)}}{\Delta\tau} \right) \quad (57)$$

Of interest in this equation are the components of the current changes in the spatial direction of the transient excitation, which is the a-axis when u_1 and u_4 are used, see Fig. 40. Therefore, after multiplying (57) by the inverse of the leakage inductance tensor (35) and taking the a-component of the result, we obtain

$$\Delta i_a^{(u_4)} - \Delta i_a^{(u_1)} = \left[(l_{\sigma d} + l_{\sigma q}) - (l_{\sigma d} - l_{\sigma q}) \cos 2\delta \right] u_s \Delta\tau \quad (58)$$

where the Δi_a are the respective changes of the a-phase current, and u_s is the magnitude of the switching state vectors.

Similar expressions are obtained for the changes Δi_b following transient excitations by u_3 and $u_6 = -u_3$, and Δi_c for excitations by u_5 and $u_2 = -u_5$, [2].

The respective phase current changes are added, aligning them with the real axis by the respective weights 1, a^2 and a

$$f = \frac{2}{3} \left[\begin{array}{l} \Delta i_a^{(u_1)} - \Delta i_a^{(u_4)} + a^2\left(\Delta i_b^{(u_3)} - \Delta i_b^{(u_6)}\right) \\ + a\left(\Delta i_c^{(u_5)} - \Delta i_c^{(u_2)}\right) \end{array} \right] \quad (59)$$

The result is a vector that has the estimated field angle in its argument,

$$f = \frac{1}{2}\left(l_{\sigma d} - l_{\sigma q}\right) u_s \Delta\tau\, e^{\,j\left(2\hat{\delta}+\pi\right)} \quad (60)$$

which can be proven by inserting the respective current changes into (59).

The vector $f(\Delta i_s)$ is computed on-line from the measured current changes. Its argument is twice the field angle, phase
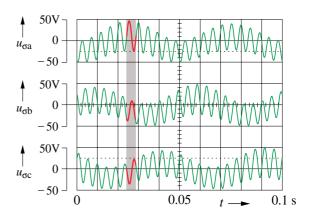

Fig. 42. Phase components of the anisotropy signal u_σ. The highlighted cycles of the rotor bar anisotropy signal form a balanced three-phase system.
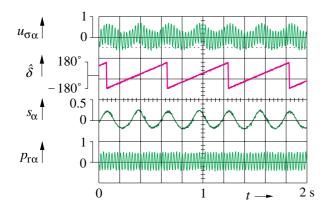
Fig. 43. Compensation of the saturation effect. From top: phase a component of the anisotropy signal, estimated field angle $\hat{\delta}$, acquired signal p'_α, saturation component s_α, extracted position signal p_α, recorded at 50 rpm

shifted by the constant displacement π. Hence

$$\hat{\delta} = \frac{1}{2}\left(arg(\boldsymbol{f}) - \pi\right) \qquad (61)$$

represents the estimated field angle. The controlled machine should have closed rotor slots. The slot covers shield the rotor bars from the high-frequency leakage fields and thus reduce, but not completely eliminate, the disturbance caused by the slotting anisotropy.

6.6.2 Instantaneous rotor position measurement

While the rotor slot anisotropy acts as a disturbance to the field angle identification methods, this anisotropy can be exploited to identify the rotor position angle. Magnetic saturation then takes the role of the disturbance. The method developed by *Jiang* [33] and *Pan* [34] relies on the instantaneous measurement of an anisotropy signal derived from the terminal voltages at the feeding inverter [35], and the starpoint potential of the machine.

As previously explained, an anisotropic rotor introduces an unbalance to the phase values of the total leakage inductances since the number of rotor slots per pole pair is not a multiple of three. The unbalance is reflected in the zero sequence voltage of a star-connected stator winding. This is obvious from the stator voltage equation

$$\boldsymbol{u}_s = \boldsymbol{l}_\sigma \frac{d\boldsymbol{i}_a}{d\tau} + \boldsymbol{u}_i \qquad (62)$$

since

$$u_{ia} + u_{ib} + u_{ic} = 0 \qquad (63)$$

and also

$$i_a + i_b + i_c = 0 \qquad (64)$$

and consequently

$$\frac{di_a}{d\tau} + \frac{di_b}{d\tau} + \frac{di_c}{d\tau} = 0 \qquad (65)$$

It is now assumed that the switching state vector changes. The resulting current change $d\boldsymbol{i}_{tr}/d\tau$ induces the transient volt-

ages $l_{\sigma a} di_a/d\tau$ in stator phase a, $l_{\sigma b} di_b/d\tau$ in phase b, and $l_{\sigma c} di_c/d\tau$ in phase c. Since the three leakage inductance values are different from each other, and (63) through (64) hold, the zero sequence voltage

$$u_\sigma = u_a + u_b + u_c \qquad (66)$$

assumes a nonzero value. Equation (66) defines the anisotropy signal u_σ, which is acquired – immediately after a commutation is completed – by measuring and adding the phase voltages u_a, u_b, and u_c.

To investigate the properties of the anisotropy signal u_σ (66), equations (62) through (65) are solved following a transient generated by switching state $\boldsymbol{u}_1$, or $\boldsymbol{u}_4 = -\boldsymbol{u}_1$, which yields

$$u_\sigma^{(1,4)} = \pm u_d \frac{l_{\sigma a}\left(l_{\sigma b} + l_{\sigma c}\right) - 2l_{\sigma b}l_{\sigma c}}{l_{\sigma a}l_{\sigma b} + l_{\sigma b}l_{\sigma c} + l_{\sigma a}l_{\sigma c}} + u_{\sigma i}, \qquad (67)$$

where u_d is the dc link voltage. In (67), the positive sign associates to $\boldsymbol{u}_1$, the negative sign to $\boldsymbol{u}_4$. The term

$$u_{\sigma i} = 3 \frac{l_{\sigma a}l_{\sigma b}u_{ic} + l_{\sigma a}l_{\sigma c}u_{ib} + l_{\sigma b}l_{\sigma c}u_{ia}}{l_{\sigma a}l_{\sigma b} + l_{\sigma b}l_{\sigma c} + l_{\sigma a}l_{\sigma c}} \qquad (68)$$

represents the contribution of the rotor induced voltages u_{ia}, u_{ib} and u_{ic}. These voltages are small at low speed and hence $u_{\sigma i}$ can be neglected in (67). The term $u_{\sigma i}$ can be eliminated at higher speed by taking the respective differences $u_{\sigma a} = u_\sigma^{(1)} - u_\sigma^{(4)}$, or $u_{\sigma b} = u_\sigma^{(2)} - u_\sigma^{(5)}$, or $u_{\sigma c} = u_\sigma^{(3)} - u_\sigma^{(6)}$, depending on which switching states are activated by the PWM control. The influence of $u_{\sigma i}$ at higher speed is discussed in [34].

Measured anisotropy signals u_σ are displayed in Fig. 42. The signals exhibit favorable characteristics:

• The waveforms of the rotor slot related anisotropy components, which are the high-frequency oscillations, are almost sinusoidal. Their phase angles are therefore in linear proportion to the rotor position angle.

• The waveforms do not exhibit an offset as the phase leakage inductance values $l_{\sigma a}$, $l_{\sigma b}$, and $l_{\sigma c}$ do.

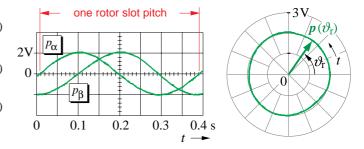The formal reason for these favorable properties is in the

Fig. 44: Measured components p_α and p_β, and the trajectory $\boldsymbol{p}(\vartheta_r)$ of the complex rotor position vector, recorded over one rotor slot pitch (12.9° motor shaft angle) at 300 rpm
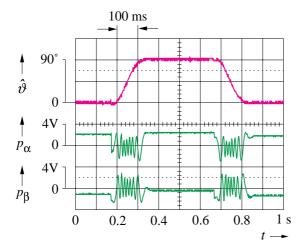
Fig. 45. Sensorless position control showing a repetitive motor shaft displacement of ±90° at 120% rated transient torque; traces from top: motor shaft angle ϑ, rotor position signals p_α and p_β; constant values indicate zero stator frequency

nonlinear mapping of the phase leakage inductances on the anisotropy signal expressed by (67). The summing of the phase voltages in (66) further eliminates all nonsignificant large fundamental components, and the offset as well. Small changes in the phase inductance values, caused by the rotor anisotropies, therefore transform to a balanced ac signal having a remarkable amplitude of around 50 V. This establishes a very high signal-to-noise ratio.

The three signals $u_{\sigma a}(\vartheta_r)$, $u_{\sigma b}(\vartheta_r)$, $u_{\sigma c}(\vartheta_r)$ form a symmetrical three-phase system. This permits defining a complex rotor position vector

$$\boldsymbol{p}'(\vartheta_N) = \frac{2}{3}\left(u_{\sigma a}(\vartheta_r) + a\, u_{\sigma b}(\vartheta_r) + a^2 u_{\sigma c}(\vartheta_r)\right)$$
$$= p_\alpha + \mathrm{j}p_\beta \tag{69}$$

The important information contained in $\boldsymbol{p}'(\vartheta_r)$ is the angular
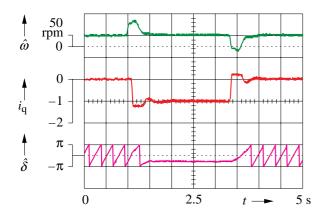

Fig. 46. Persistent operation at zero stator frequency with 120% rated torque applied. The steady-state processes are initiated and terminated by transient commands; traces from top: estimated speed $\hat{\omega}$, normalized torque-building current i_q, field angle $\hat{\delta}$

rotor position ϑ_r as referred to $1/(n_{rp})^{th}$ of a mechanical revolution, being expressed by the phase angle of $\boldsymbol{p}'(\vartheta_r)$, which is ϑ_r. The magnitude of $\boldsymbol{p}'(\vartheta_r)$ bears no significance.

The rotor position ϑ within one mechanical revolution of the motor shaft is obtained by incrementing (or decrementing at reversed rotation) a modulo-(pn_{rp}) counter whenever a full cycle of ϑ_r is completed. Hence the incremental rotor position within a full revolution is

$$\vartheta = (2\pi C_r + \vartheta_r)/n_{rp} \tag{70}$$

where C_r is the state of the counter. The equation illustrates the nature of this sensorless position measurement, which is absolute and of high resolution within one slot pitch, and incremental in that the angular displacements of the individual rotor slots are counted. It is quasi-instantaneous and hence can be obtained at high dynamic bandwidth.

To establish a sensorless speed control system, the field angle δ is derived from the rotor position angle ϑ (70) by adding the slip angle obtained from the condition for rotor field orientation (6)

$$\hat{\delta} = \frac{\vartheta_r}{n_{rp}} + \frac{l_m}{\hat{\tau}_r}\int \frac{i_q}{\psi_{rd}}d\tau, \tag{71}$$

Also the rotor speed $\omega_m = \omega_s - \omega_r$ is determined from (6).

The field angle (71) can further serve to eliminate the saturation induced disturbance of the position signals. Saturation introduces the low-frequency components that superimpose on the measured signals u_σ in Fig. 42. Other than the rotor position which synchronizes with the position angle ϑ, the saturation components are in synchronism with the field angle δ. A set of multiplexed adaptive spatial low-pass filters, addressed in synchronism with the estimated field angle $\hat{\delta}$, extracts a saturation vector $\boldsymbol{s}(\hat{\delta})$ from the distorted signal $\boldsymbol{p}'(\vartheta_r)$, permitting to calculate an undisturbed position signal $\boldsymbol{p}(\vartheta_r) = \boldsymbol{p}'(\vartheta_r) - \boldsymbol{s}(\hat{\delta})$, [34]. The α-component of this signal is shown in the lowest trace of Fig. 43. Waveforms of the compensated position vector $\boldsymbol{p}(\vartheta_r)$, recorded at 300 rpm, are shown in Fig. 44.

Rotor position acquisition is possible at sampling rates of several kHz [34]. Dead-time phenomena have no detrimental effect. The spatial resolution and the signal-to-noise ratio are very high. This permits implementing precise incremental positioning systems for high dynamic performance. However, the incremental position is lost at higher speed when the frequency of the position signal becomes higher than twice the sampling frequency. Even so is positioning possible while operating up to double rated speed if a fundamental model is used in parallel that estimates the speed and the direction of rotation.

The oscillogram Fig. 45 shows a positioning cycle that exhibits maximum dynamics at 120% rated torque. The high magnetic saturation during the acceleration intervals temporarily reduces the amplitude of the position signals; the posi-

tion accuracy remains unaffected, since the relevant information is contained in the phase angles.

Sustained operation at zero stator frequency, combined with high dynamic performance at 120% torque overload is demonstrated in Fig. 46. In this experiment, the machine is operated at speed control with the speed reference set to 50 rpm. This value corresponds to the slip speed at 120% torque overload. While operating initially without load, the system is subsequently subjected to a step change of 120% torque in the direction of rotation. Such disturbance causes a transient increase in speed which is compensated by a steeply falling torque current i_q. The dynamic peak torque is 150% rated, which lets the motor regain its set speed immediately after the transient. The control masters the subsequent steady-state at zero stator frequency and 120% overload. Note that the field angle $\hat{\delta}$ in the lower curve does not change. Even at zero stator frequency does the system maintain its full dynamic ability, which will persist for an infinite time. The torque current i_q reacts instantaneously to the sudden removal of the external torque, reestablishing the set speed after a short transient speed drop. The maximum speed in the experiments was around 1000 rpm.

7. CONCLUSION

Sensorless control of induction motors is an attractive technology which has gained considerable market share in the past few years. Improvements are still sought with respect to simplicity, robustness and accuracy at very low speed. Two basic methodologies are competing to reach this goal. Algorithms that rely on the fundamental machine model excel through their simplicity, even when more sophisticated and detailed models are implemented for the components of the drive system. Additional hardware for the acquisition of the machine terminal voltage can be spared when modelling the inverter as a nonlinear component. Immunity to noise and offset drift is achieved by appropriate estimators. Parameter estimation schemes adapt the control system to any given machine.

Most critical conditions exist around zero stator frequency. The induction motor then becomes an unobservable system. Nevertheless can the fundamental machine model provide sustained controllability in this region for a larger time duration. It is required, though, that the offset drift does not change while the condition of close to zero stator frequency prevails.

Such limitations are not experienced when the anisotropic properties of the machine are exploited. The injection of additional high-frequency signals subjects the motor to transient conditions. Its response bears the spatial orientations of the anisotropies as a signature. Machines with closed rotor slots exhibit only one anisotropy which is caused by magnetic saturation. Its angular orientation, the field angle, can be determined, provided that load-dependent deviations are identified and compensated. Open slot rotors exhibit spatially discrete

magnetic structures in addition. Identifying this anisotropy yields a high-resolution rotor position signal of high dynamic bandwidth; the influence of the saturation anisotropy must be adaptively compensated.

It is the nonlinear properties of two different anisotropies, of which only one can be utilized at a time, which makes carrier injection methods for sensorless control highly sophisticated. Their design is not general as it must match the properties of the particular drive motor. In addition, the nonlinearities of the PWM inverter require identifying complex and time-variable compensation functions for every operating point. These nonlinearities do not interfere when the transient excitation of the inverter switching are exploited to acquire the anisotropy signals.

Model based estimation methods, on the other hand, enable zero stator frequency operation for extended time periods; even so, permanent stability cannot be guaranteed. Nevertheless is the less complicated implementation of model based methods a distinct advantage which makes these the good choice for most applications. If long-term stability at zero stator frequency is an issue, anisotropic properties of the machine may be exploited as a temporary addition.

8. REFERENCES

1. K. Rajashekara, A. Kawamura, and K. Matsuse, (Editors), „Sensorless Control of AC Motors", *IEEE Press Book*, 1996.
2. J. Holtz: Sensorless Control of Induction Motors, „*Proceedings of the IEEE*", Vol. 90, No. 8, Aug. 2002, pp. 1358-1394.
3. J. Holtz, „The Representation of AC Machine Dynamics by Complex Signal Flow Graphs", *IEEE Transactions on Industrial Electronics*, Vol. 42, No. 3, June 1995, pp. 263-271.
4. C. Schauder, „Adaptive Speed Identification for Vector Control of Induction Motors without Rotational Transducers", *IEEE Industry Applications Society Annual Meeting,* San Diego Ca 1989, pp. 493-499.
5. T. Ohtani, N. Takada, and K. Tanaka, „Vector Control of Induction Motor without Shaft Encoder", *IEEE Transactions on Industry Applications,* Vol. 28, No. 1, Jan/Feb. 1992, pp. 157-165.
6. Y. Murai, T. Watanabe and H. Iwasaki, „Waveform Distortion and Correction Circuit for PWM Inverters with Switching Lag-Times", *IEEE Transactions on Industry Applications*, Vol. IA-23, No. 5, pp. 881-886, Sept./Oct. 1987.
7. Th. Frenzke, F. Hoffman, and H. G. Langer, „Speed Sensorless Control of Traction Drives – Experiences on Vehicles", *8th European Conference on Power Electronics and Applications EPE*, Lausanne, (1999), on CD ROM.
8. J. Holtz and J. Quan, „Sensorless Vector Control of Induction Motors at Very Low Speed using a Nonlinear Inverter Model and Parameter Identification", *IEEE Transactions on Industry Applications*, Vol. 38, No. 4, July/Aug 2002, pp. 1087-1095.
9. H. Kubota, K. Matsuse, and T. Nakano, „DSP Based Speed Adaptive Flux Observer of Induction Motor", *IEEE Transactions on Industry Applications,* Vol. 29, No. 2, Apr/Mar. 1993, pp. 344-348.
10. J. Maes and J. A. Melkebeek, „Speed-Sensorless Direct Torque Control of Induction Motors using an Adaptive Flux Observer", *IEEE Transactions on Industry Applications,* Vol. 36, No. 3, May/June 2000, pp. 778-785.
11. C. Lascu, Ion Boldea and F. Blaabjerg, „Very Low Speed Sensorless Variable Structure Control of Induction Machine Drives

without Signal Injection", *IEEE International Electric Machines and Drives Conference IEMDC*, Madison/Wi., USA, June 1-4, 2003, on CD ROM.

12. J. Holtz and A. Khambadkone, „Vector Controlled Induction Motor Drive with a Self-Commissioning Scheme", *IEEE Transactions on Industrial Electronics*, 1991, pp. 322-327.

13. H. Kubota and K. Matsuse, „Speed Sensorless Field Oriented Control of Induction Motor with Rotor Resistance Adaptation", *IEEE Transactions on Industry Applications,* Vol. 30, No. 5, Sept/Oct. 1994, pp. 1219- 1224.

14. J. Holtz and J. Quan, „Drift and Parameter Compensated Flux Estimator for Persistent Zero Stator Frequency Operation of Sensorless Controlled Induction Motors", *IEEE Transactions on Industry Applications*, Vol. 39, No. 4, July/Aug. 2003, pp. 1052-1060.

15. M. W. Degner and R. D. Lorenz, „Using Multiple Saliencies for the Estimation of Flux, Position and Velocity in AC Machines", *IEEE Transactions on Industry Applications*, Vol. 34, No. 5, Sept/Oct. 1998, pp. 1097-1104.

16. J. Cilia, D. M. Asher and K. J. Bradley, „Sensorless Position Detection for Vector Controlled Induction Motor Drives Using an Asymmetric Outer-Section Cage", *IEEE Transactions on Industry Applications*, Vol. 33, No. 5, Sept/Oct 1997, pp. 1162-1169.

17. F. Briz, A. Diez, and M. W. Degner, „Dynamic Operation of Carrier-Signal-Injection-Based Sensorless Direct Field-Oriented AC Drives", *IEEE Transactions on Industry Applications*, Vol. 36, No. 5, Sept/Oct. 2000, pp. 1360-1368.

18. J. Holtz, „Sensorless Position Control of Induction Motors – an Emerging Technology", *IEEE Transactions on Industrial Electronics*, Vol. 45, No. 6, Nov/Dec. 1998, pp. 840-852.

19. N. Teske, G. M. Asher, M. Sumner, and K. J. Bradley, „Suppression of Saturation Saliency Effects for the Sensorless Position Control of Induction Motor Drives under loaded Conditions", *IEEE Transactions on Industrial Electronics*, Vol. 47, No. 5, Sep/Oct. 2000, pp. 1142-1149.

20. C. Caruana, „Sensorless Vector Control of Cage Induction Machines using Signal Injection Techniques", Ph.-D. Dissertation, *University of Nottingham*, 2004.

21. J. Holtz, „On the Spatial Propagation of Transient Magnetic Fields in AC Machines", *IEEE Transactions on Industry Applications*, Vol. 32, No. 4, July/Aug. 1996, pp. 927-937.

22. N. Teske, G. M. Asher, K. J. Bradley, and M. Sumner, „Analysis and Suppression of Inverter Clamping Saliency in Sensorless Position Controlled of Induction Motor Drives", *IEEE Industry Applications Society Annual Meeting*, Chicago, Sept. 30 - Oct. 4, 2001, on CD-ROM.

23. J.-W. Choi, S.-K. Sul, „A New Compensation Strategy Reducing Voltage/Current Distortions in PWM VSI Systems Operating with Low Output Voltages", *IEEE Transactions on Industry Applications*, Vol. 31, No. 5, Sept/Oct. 1995, pp. 1001-1008.

24. N. Teske, G. M. Asher, K. J. Bradley, and M. Sumner, „Encoderless Position Control of Induction Machines", *9th European Conference on Power Electronics and Applications EPE*, Graz/Austria, (2001), on CD ROM.

25. H. Kim, M. C. Harke, and R. D. Lorenz, „Sensorless Control of Interior Permanent Magnet Machine Drives with Zero-Phase-Lag Position Estimation", *IEEE Transactions on Industry Applications*, Vol. 32, No. 4, July/Aug. 1996, pp. 927-937.

26. A. Consoli, G. Scarcella and A. Testa, „Speed- and Current-Sensorless Field-Oriented Induction Motor Drive Operating at Low Frequencies", *IEEE Transactions on Industry Applications*, Vol. 40, No. 1, Jan/Feb. 2004, pp. 186-193.

27. J.-I. Ha and S.-K. Sul, „Sensorless Field-Oriented Control of an Induction Machine by High-Frequency Signal Injection", *IEEE Transactions on Industry Applications*, Vol. 35, No. 1, Jan/Feb. 1999, pp. 45-51.

28. B.-H. Bae, G.-B. Kim and S.-K. Sul, „Improvement of Low Speed Characteristics of Railway Vehicle by Sensorless Control Using High Frequency Injection", *IEEE Industry Applications Society Annual Meeeting*, Rome/Italy, Oct. 2000, on CD ROM.

29. M. Linke, R. Kennel, and J. Holtz, „Sensorless Speed and Position Control of Permanent Magnet Synchronous Machines", *IECON, 28th Annual Conf. of the IEEE Industrial Electronics Society*, Sevilla/Spain, 2002, on CD ROM.

30. M. Linke, „Injection of Alternating Carrier Signals for Sensorless Control of Revolving Field Machines (in German)", *Ph.-D. Dissertation*, Wuppertal University, 2003.

31. J. Jiang and J. Holtz, „High Dynamic Speed Sensorless AC Drive with On-Line Parameter Tuning and Steady-State Accuracy", *IEEE Transactions on Industrial Electronics*, Vol. 44, No. 2, 1997, pp. 240-246.

32. M. Schroedl, „Sensorless Control of AC Machines at Low Speed and Standstill based on the Inform Method", *IEEE Industry Applications Society Annual Meeting*, Pittsburgh, Sept. 30 - Oct. 4, 1996, pp. 270-277.

33. J. Jiang, „Sensorless Field Oriented Control of Induction Motors at Zero Stator Frequency" (in German), *Ph.-D. Dissertation*, Wuppertal University, 1999.

34. J. Holtz and H. Pan, „Elimination of Saturation Effects in Sensorless Position Controlled Induction Motors", *IEEE Transactions on Industry Applications*, Vol. 40, March/April 2004.

35. J. Holtz and H. Pan: Acquisition of Rotor Anisotropy Signals in Sensorless Position Control Systems. *IEEE Industry Applications Society Annual Meeting*, Utah, Oct. 12-16, 2003.